

“Nano-Material and Structural Engineering for Thermal Highways”

14 June 2013

Ki-Bum Kim (KPI), Jimmy Xu (USPI), Ho-Ki Lyeo (Co-PI)

- e-mail address : kikum@snu.ac.kr, jimmy_xu@brown.edu, hklyeo@kriss.re.kr
- Institutions : Seoul National University, Brown University, and KRISS

Period of Performance: 06/15/2010 – 06/14/2013

Abstract

The AOARD-KRF ‘thermal management’ project has led to several developments and breakthroughs driven by collaborative efforts between the Korean groups (Seoul National University and KRISS) and the group at Brown University. Two main objectives were set for the project: improvement of thermoelectric efficiency and demonstration of “thermal diodes” with heat-flow rectification. Both objectives were successfully met, and in fact, exceeded.

One breakthrough – thermal-voltage imaging with unprecedented atomic resolution that exceeds classical limits is particularly noteworthy. It was unanticipated at the start but propelled by growing interests arising from this effort. It will likely extend its impact beyond thermal management into basic sciences for years to come.

Several strategies for improving thermal functionality in electronic materials were implemented via AIPEL patterning, AAO-templated nanomesh formation and atomic-layered doping. Thermal rectification effects have been ascertained by engineering into the structure phase-changing and strongly temperature dependent materials. An ultrathin (~40nm) film that is infrared (heat) reflecting, light-transmitting (>90%), highly conductive (~1000 S/cm) and also EMI-shielding (>20dB) stands out as another example outcome of the exploration of an atomic-layer engineering approach. It could lead to defense and civilian applications in near term. A novel concept of self-regulated cooling, inspired by nature (e.g. human skin sweating), was implemented, tested, and proven to be effective. This success, however still preliminary, opens a pathway to explorations of wearable, scalable, distributed, self-powered cooling and temperature regulation, as well as to its underlying science of phase-transitions in nano-capillary fluidics.

Details of key findings have been documented in some 10 publications, including one to appear in Nature Materials, one patent application, and several more to follow.

Introduction

Thermal management and heat-flow control represents a key issue to electronic industry's ability to continue its advance, which has been so great that for better or for worse it has changed out civilization.

Ability to control heat flow on microchips is somewhat similar to the construction of highways with road intersections, one-way paths, and bridges. Generation and transport of heat present both a limitation and an opportunity of increasingly great importance in many systems, ranging from microelectronics to aircrafts. In fact the importance of these issues is so great that it has been stated in Intel and AFRL that, "We have hit the thermal wall! System design alone can no longer handle the heat." Both aerospace and electronics industries need new materials that "engage down to molecules to manage the waste heat". Current bulk materials are no longer sufficient to provide necessary thermal management, and the future is likely in composite and structured nanomaterials. Just as on macroscale, system design was able to provide thermal control by heat sinks, fans, liquid cooling, etc. nanomaterial design could incorporate nano heat sinks and nano channels as an intrinsic part of composite material. The research in this area has already shown great potential with carbon nanotube microfin architectures used as a heat sink device [1,2]. While incorporating macroscale thermal management concepts on a micro and nanoscale is a new undertaking, one may still profitably rely on well-understood heat conduction mechanisms for thermal management.

Another avenue that is exciting and largely unexplored is the incorporation of atomic and quantum size effects for thermal control. These effects include phonon confinement and anharmonic phonons and conversions. Here, the main effect of using nanomaterials is to present a low-dimensional system where quantum effects dominate the thermal transport. In addition, nano-engineering could enable thermal properties otherwise unavailable in the bulk phase, for example, a decrease in thermal conductance along with an increase in electronic conductance when diameter falls below a threshold value. Since a phonon's coherence length could be much larger than that of an electron, the phonon properties of low-dimensional systems, such as the phonon frequency, group-velocity, spectral density, as well as the strength of the interaction with electrons, can be controllably altered by nanoscale structural, material and surface engineering. While there are numerous heat management issues that have to be addressed, we focused on two problems of interest: improvement of thermoelectric efficiency and the exploration of mechanisms for thermal rectification.

We sought to develop devices and materials capable of directional thermal transport, thermal rectification and improved thermoelectric efficiency. The following approaches were proposed for improving thermoelectric efficiency:

- 1-D nanowire, nano-channel and nanowire arrays by projection e-beam lithography.
- 2-D lateral nano-networks for controlled planar thermal transport.
- 3-D vertical nanowire and nanochannel (nanotube) array platforms.

Further, we proposed several mechanisms for thermal rectification, of which we focused on two in this 3-year duration:

- Rectification using heat-actuated thermal contact via thermal expansion.
- *Rectification based on junction of material with dissimilar thermal conductivities.*
- *Rectification based on anharmonic heat transport.*
- Rectification based on phonon confinement.

In addition to the proof-of-concept technology development, the team also aimed to address and establish a good understanding of a number of basic scientific issues arising from phonon confinement, and anharmonic phonons and conversion in homo and heterojunctions. Moreover, engineering approaches were refined or invented to yield improvements in thermoelectric efficiencies and achievement of thermal rectification. Specifically, these objectives have been pursued along with the development of necessary nano-materials and nanostructures as building blocks, including temperature-dependent-phonon-transporting and phase-changing polymers, semimetallic Bi nanowires, nanomesh-structured carbon nanotube films, and transparent conductive thermoelectric oxides. Of these, the detailed motivation,

results, and strategy of each target material/nanosystem are reported in the following sections.

Experimental methodologies

a) Thermal rectification using non-linear temperature dependence of thermal conductivity

The proposed thermal diode concept was implemented in a specific device design, which was then fabricated from a series combination of PNIPAM and PDMS polymers. The strong temperature dependence of thermal conductivity in PNIPAM and the designed structural asymmetry resulted in a non-linear heat flow through the device, preferentially in one direction versus the other. In its hydrophilic phase, water in the PNIPAM is bound and immobilized by hydrophilic groups in the polymer chains, but when the temperature rises above the phase transition temperature water becomes unbound and the polymer change its conformation and hydrophilicity such that the water molecules are expelled out while the polymer shrinks in volume. Convection current through the water creates an additional and more conducive heat transfer pathway from one end of the device to the other, lowering its overall thermal resistance. This decrease in thermal resistance allows higher heat flux or current to flow.

The configuration of the device and experiment is shown in Figure 1. The basic concept and device configuration is generic enough that can be adapted to many other material pairs, including semiconductors. In this specific example, the device is constructed by filling an insulating cylindrical tube with equal volumes of PDMS and PNIPAM, which is then sandwiched between two pieces of silicon. In experiments, one side is placed in contact with a constant temperature heat bath at 0°C, and the other side is placed in contact with a resistive heating element, consisting of three 150 Ω resistors in parallel. The power to the heater was increased incrementally and the temperature difference was measured once a steady state was reached. The forward operation of the diode is when the hydrogel side is heated, and the reverse mode is when the PDMS side is heated. In the reverse mode, the temperature drop over the low-thermo-conductivity PDMS is so large that PNIPAM phase change does not occur until the heating power exceeds its ‘break-down’ threshold, but when heat is applied directly to the hydrogel side, the phase change occurs and reduces the total thermal resistance. Separation of water and shrinkage of PNIPAM was observed as represented in Figure 1.

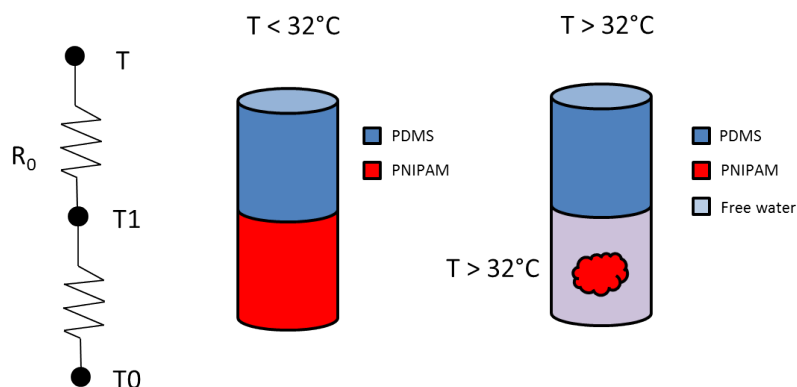


Figure 1. Diagram of thermal diode set up. In the forward direction, T_0 is held at constant 0°C and T is gradually increased with increasing power supplied to the resistive heater. The device is allowed to reach steady state and the temperature difference between the plates is measured.

b) Self-regulated cooling via synthetic sweating structures

For self-regulated cooling as that built in our skin, a synthetic sweating nanocomposite device was developed and tested for thermal regulation applications. The design is inspired by the natural mechanism in the skin of humans and other mammals where self-maintaining a constant temperature is vital to the survival of the organism, especially in harsh climates. The primary self-regulation mechanism in the device design relies on phase-transitions through a combined action of a polymer phase-transition, capillary transport of coolant to the vaporization surface, and then the liquid-vapor phase transition of nano- and micro-droplets modified by the size-dependent Laplace pressure.

The less evident but no less critical self-regulated secretion of coolant (e.g. water) and subsequent transport to the surface are the interesting control parameters that can be accessed and controlled through structural and material engineering. Just like our skin, the separation of the coolant reservoir from the vaporization surface and their connection via capillary channels are also essential. Without them, direct evaporation of coolant could happen when cooling is no longer needed, or worse when heat is to be preserved, for example, when sleeping on a windy hilltop. This self-regulated secretion function is implemented through the use of a phase-change polymer hydrogel that stores the absorbed coolant in its polymer matrix until the temperature rises to a pre-set threshold temperature, at which it secretes coolant for extraction by the capillary tube driven by Laplace force to exterior surface. There are multiple polymer options for this purpose but for better maturity and familiarity we opted for a well-known polymer hydrogel, poly(N-isopropylacrylamide), or PNIPAM, in our experiment. Likely for similar considerations of availability, cost, and maturity, Rotzetter *et al.*, also took advantages of this hydrogel in an independent experiment on the feasibility of rooftop cooling. In our micro-device design and implementation, the PNIPAM hydrogel is housed in mini-cells which are covered with a porous anodized aluminum oxide (AAO) membrane that is compatible to most if not all semiconductor electronics chips and has densely-packed ($10^9/\text{cm}^2$) nano-channels of 100 nm in diameter perforating the membrane. These nano-channels serve as capillary conduit to draw water expelled from the PNIPAM by the Laplace pressure to the exterior surface of the AAO membrane.

The motivation behind using PNIPAM is not only its well-known and studied properties but also it closely mimics the function of the sweat gland. Without modification, the common PNIPAM hydrogels exhibit a phase change as temperature increases above approximately 32 °C, at which as mentioned earlier it begins to shrink and expel its water content. Human body responds in a similar way in response to small increases in internal temperature above 37 °C, at which point cutaneous blood vessels in the skin dilate (polymer shrinks, flow increases), increasing the blood flow to the skin, causing increased heat conduction and visible redness. Then, sweat glands secrete water, pores dilate, and the sweat rises to the skin's surface to form an evaporating droplet, which removes heat from the body due to the latent heat of vaporization of water [3]. The dynamic ability of skin to self-regulate sweat secretion, control thermal resistance and establish an array of evaporating droplets are key features that have guided us and others into this investigation using sweating as a guiding principle. The formation of micro/nanodroplets provides us another engineering opportunity to optimize the design to trade off cooling rate (J per unit time) with the cooling efficiency (J per unit volume of coolant).

Experimental demonstrations of synthetic sweating are critical to validation of the concept and the assessment of its potential applications. Understanding its underlying physics would offer guidance to device designs and optimization. For the former, our experiments along with that of Rotzetter *et al.* offered independent evidences of proof. For the latter, we sought to develop a physical model for the heat and mass transfer in a synthetic sweating device structure, with which one could then hope to develop better or more optimized device structure designs for specific applications.

The heating process of a warm body covered with a synthetic sweating composite is shown in Figure 2, showing three characteristic regimes. Upon application of a constant heat

flux to the body, the body temperature initially rapidly rises, followed by a long lasting plateau of nearly constant temperature. This nearly constant temperature plateau, even under constant heating, resembles what the body does and is a result of PNIPAM hydrophilicity phase-transition (in the form of polymer chain collapse at the transition temperature and subsequent water release). The efficient heat removal process of liquid-vapor phase-transition combines PNIPAM hydrophilicity-phase change to reproduce the self-regulated cooling seen in nature's sweating process. Additionally, a thermal conduction path forms to aid the heat dissipation when water fills the pores, effectively increasing the thermal conductivity from source to ambient. A physical model was developed to capture the dynamical behavior of the synthetic sweating mechanism for future applications that could reach beyond cooling into realms such as distributed engine self-lubrication, fuel cell supply and water removal, and drug delivery or biofluid sample extraction.

The heating and cooling process of the bio-mimicking cooling structure could be analyzed in three regimes. Beginning at room temperature, a constant heat flux, Q_0 , is applied from the bottom. In the first regime, the rise in temperature is inversely proportional to the thermal mass and heat capacity as most of the heat flux works to raise the temperature of the composite, with negligible heat transfer occurring at the interface with the environment. Heat conduction through the composite is slow due to the higher thermal resistances of the empty capillary channels and the hydrogel below its phase transition temperature. The polymer matrix inhibits the mobility of water in the composite via strong binding to the polymer's exposed hydrophilic groups [4], preventing convection of water within the composite in the swollen state. The heat transfer coefficient at the composite-air interface is also assumed to be orders of magnitude below that of convection of water in our model. These assumptions are consistent with the experimental observations. This initial temperature rise regime comes to an end when the polymer reaches its phase transition temperature, and begins to expel its water.

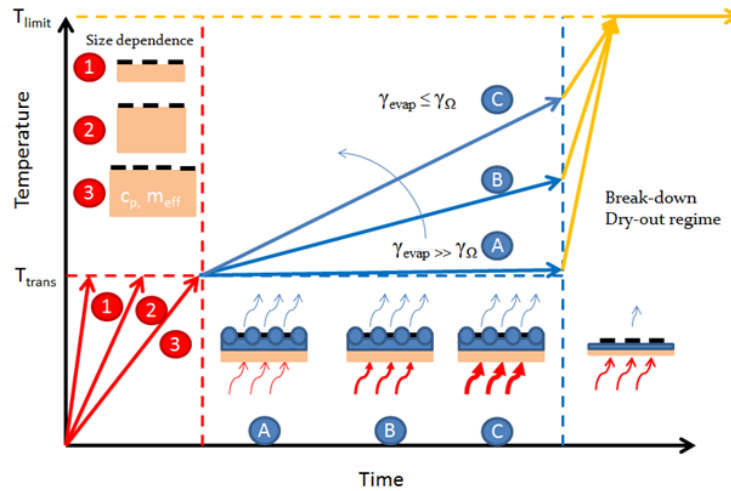


Figure 2. Breakdown of experimental results during each phase of operation.

When water is expelled from the hydrogel, it is quickly drawn into the capillary channels, creating a thermal conduit between the composite and the environment that was poorly conductive before with slow diffusion of vapor in the porous layer. Free convection of water at the boundary becomes possible in addition to the vaporization of droplets occurring in the pores. This regime is characterized by a long lasting constant temperature in the composite and at the interface with the air, which was measured in our experiment.

Lastly, we observed a dry-out regime in our experiment when all the water was expelled from the hydrogel and the enhanced heat transfer at the boundary ceases, causing further rise in the measured temperature.

An experimental test of this model was set up, as shown in Figure 3. The findings are in support of the model. In this experiment, 25 mg of dry PNIPAM was hydrated overnight with 250 μL of water and placed in a heating device. The device consisted of a resistive heating element attached to the underside of a silicon chip with a PDMS cell containing the PNIPAM above. The PNIPAM was sealed inside the cell with a porous AAO membrane average pore radius of 100 nm. The heater was set to constant power and the membrane temperature was measured every 15 seconds for a period with a thermocouple at the membrane-air interface.

Before presenting a more comprehensive analysis of the self-regulated cooling process based on the analytical model, we will proceed to complete the presentation of experimental methods developed in parallel for the pursuit on the other fronts of this project.

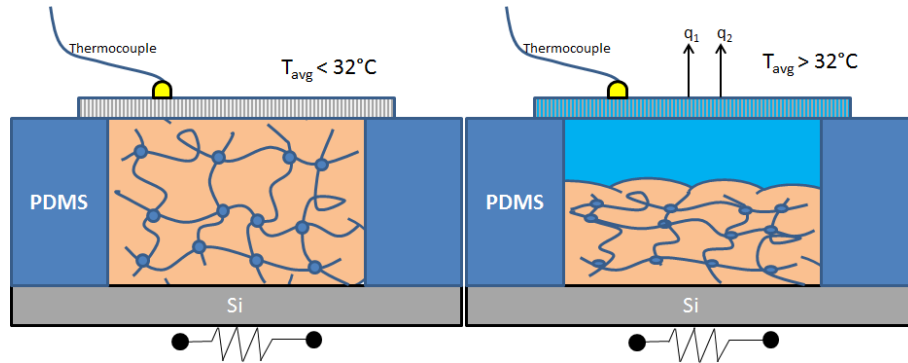


Figure 3. Schematic experimental set-up for demonstrating the synthetic sweating.

c) Electrical and thermal transport in nanostructures fabricated by AIPEL (Atomic Image Projection E-beam Lithography)

In order to fabricate highly periodic nanostructures of various dimensions and morphologies, our team utilized “AIPEL (Atomic Image Projection E-beam Lithography)” originally developed by Prof Kim’s group (Prof. Ki-Bum Kim at SNU). AIPEL is a variation of e-beam lithography which uses natural masks, consisting of high-resolution TEM images, and a parallel beam for the e-beam exposure to ensure much-higher throughput. Figure 4 illustrates schematic ray diagrams of HRTEM and AIPEL systems. Details on the AIPEL system can be found in Refs. 5 and 6.

As candidate substrates, either Si on insulator (SOI) wafers or pulsed laser deposition (PLD)-grown Bi films grown on SiO_2 (100nm) / Si wafers were used. HRTEM images of a single crystalline Si and $\beta\text{-Si}_3\text{N}_4$ were used as masks for the fabrication of straight and corrugated nanowires, respectively. Hydrogen silsesquioxane (HSQ) as a negative resist was spin coated on a target substrate and e-beam exposure was subsequently conducted on that by using AIPEL system. Next, unexposed HSQ was developed by tetramethylammonium hydroxide (TMAH) and, finally, nanopatterns were formed by reactive ion etch (RIE), as schematically shown in Figure 4.

For deposition of the PLD-Bi films, a precision PLD system was supported by Prof. Sang-Im Yoo’s group at SNU. Parameters including target-substrate distances, working pressures, and substrate temperature were varied in order to optimize electrical resistivity and surface roughness of Bi films. For electrical characterization of Bi nanowires, Agilent HP 4156C Precision Semiconductor Parameter Analyzer combined with a hot chuck-equipped probe station was utilized.

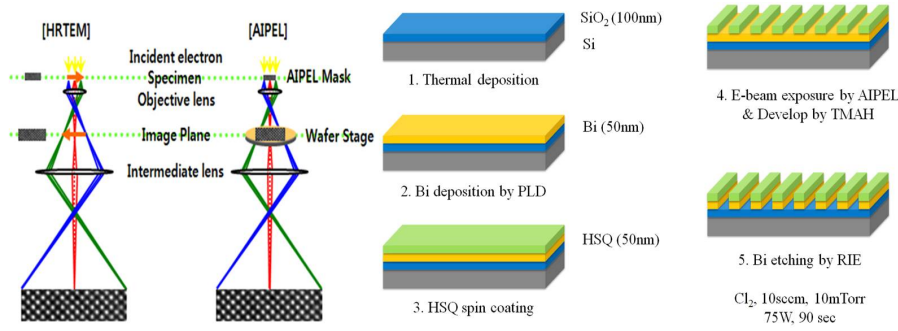


Figure 4. Ray diagrams of HRTEM and AIPEL (left), and the AIPEL process applied into a Bi thin film (right).

d) Thermoelectric power enhancement via an AAO-templated nano-patterning process

In this effort, we utilized highly ordered, highly periodic nanoporous anodized aluminum oxide (AAO) templates as hard masks for fabrication of nanomesh thermoelectric structures. Both USPI's and KPI's laboratories have accumulated experiences on preparing the AAO templates, as reflected in many of their articles [7-13] and these experiences greatly eased this pursuit.

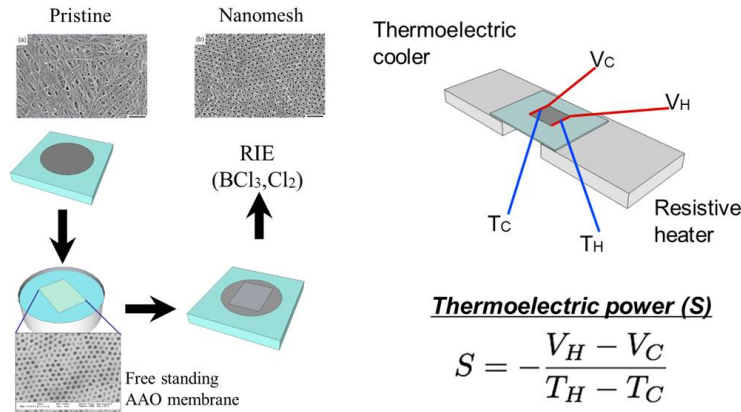


Figure 5. Schematic fabrication process of CNT nanomesh (left) and experimental setup of thermoelectric power measurement (right).

As target materials, we used thermally evaporated Bi film and CNT film formed by a membrane infiltration method. Once the target materials were deposited or delivered to substrates, the homemade AAO membranes (100 nm period and 50nm nanopores) were transferred directly atop of Bi or CNT films. After that, RIE process was conducted in order to etch exposed area, through the nanoporous holes, and finally the AAO hard mask was removed. Schematic fabrication process is illustrated in Figure 5. We note that the AAO membrane is scalable in size and dimension adjustable.

For the measurement of thermoelectric power (S), experimental setup, as shown in Figure 5, was prepared and the nanomesh samples were laid between a resistive heater (hot end) and a thermoelectric cooler (cold end). Thermovoltage (i.e. voltage difference across the both ends) and temperature difference were simultaneously measured upon variation of hot and cold end temperatures. Temperature-dependent electrical resistance measurement was performed in a cryostat at 10^{-3} Torr and with liquid nitrogen cooling.

e) Heterolayered Al-doped ZnO composites for a new platform of transparent

thermoelectrics

Heterolayered AZO composites were deposited by alternate stacking of a ZnO matrix and AlO_x atomic-doping layers, as schematically shown in Figure 6. For the deposition either ASM-Genitech GENI-MP1000 system or NCD Technology Lucida D-100 system was used. Detailed experimental conditions can be found in Refs. 14-16. Electrical conductivity was measured by Hall measurement system and thermal conductivity was measured by TDTR (Time Domain ThermoReflectance) method aided by the system in KRISS, Korea (Figure 7). MMR tech's SB-100 Seebeck measurement system (KIRSS, Korea) was introduced to investigate temperature-dependent Seebeck coefficient of AZO composites. UV-visible transmittance was measured by using Cary 5000 system (Varian). Fourier transform infrared spectrometer (Bruker Equinox 55) and vector network analyzer (HP 8510B) were used for the IR transmission and complex reflectance of microwaves, respectively. The obtained complex reflectance was sequentially converted into the microwave transmission (T) and shielding efficiency (SE) with the relation of $\text{SE} = -10 \log(T)$. In order to obtain the IR reflectance, plasma frequency and real and imaginary parts of permittivity, the Drude-Lorentz model was applied.

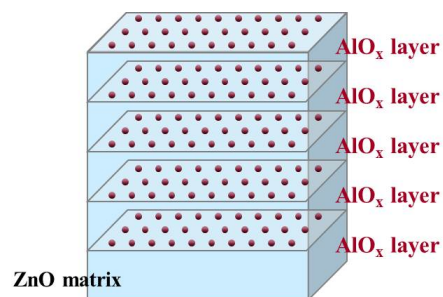


Figure 6. Schematic illustration of ALD-grown heterolayered AZO composite.

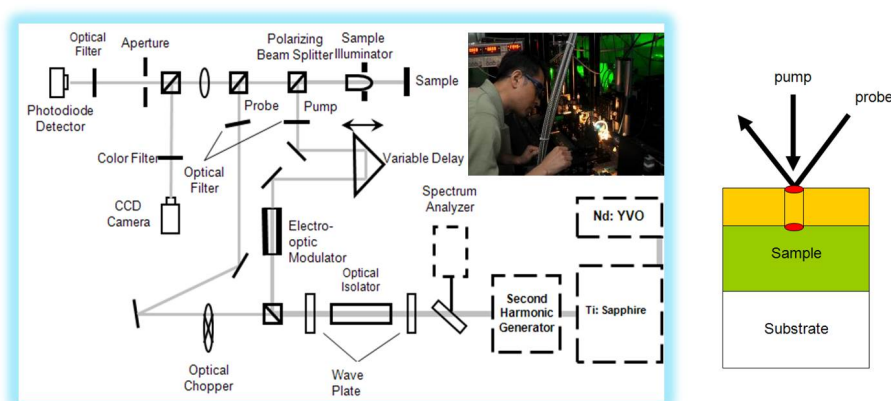


Figure 7. Principle of TDTR method. Thin Al layer ($\sim 70\text{nm}$) was coated onto samples for the thermal conductivity measurement. Pump laser is used to heat up the Al layer and probe laser detects reflectance and temperature changes of the Al layer.

f) Thermo-voltage imaging of unprecedented resolution at atomic level

Stimulated by exchanges of ideas and the need to understand thermal behavior from atomic layers down to the most fundamental level, atoms, the co-PI Dr. H-K Lyeo of KRISS championed the development of a scanning thermo-voltage measurement technique. With this technique, thermoelectric scanning measurement was performed and proved capable of detecting disorder and strain at atomic scale, through large and spatially localized electronic signatures. This method, unlike the atomic force microscope (AFM), reveals distortions in the

local electronic structure at atomic-scale. In our efforts, we have tried to image structural disorder of epitaxial graphene by using the thermoelectric scanning measurement. To develop thermoelectric scanning microscopy, we used a modified ultra-high vacuum atomic force microscope (UHV-AFM) with a gold-coated conducting probe that scans the sample in contact mode while maintaining a temperature difference between the tip and the sample [Figure 8(a)]. A localized temperature gradient is induced in the vicinity of the tip, yielding a thermoelectric voltage proportional to the local thermopower of the contact region. The primary investigation on graphene was conducted by “normal scanning”, where we collect transient thermoelectric signals at a scan time comparable to that of conventional AFMs. The thermopower image of epitaxial graphene acquired by normal scanning [Figure 8(c)] clearly shows the coexistence of three contrasted regions with different thermopower and resident features, which were identified as mono-layer, bi-layer, and tri-layer graphene (MLG, BLG, and TLG). The enormous detail in the thermopower image is absent in the simultaneously obtained topographic image, which only displays the terraced structure of the SiC substrate. The complex patterns found in each graphene layer, for example, the dark lines found in BLG, are not terrace steps but strain-related features existing within the graphene layer. The thermopower image of both MLG and BLG produce a negative thermoelectric voltage signal, which is a result of the electron doping induced by the underlying substrate.

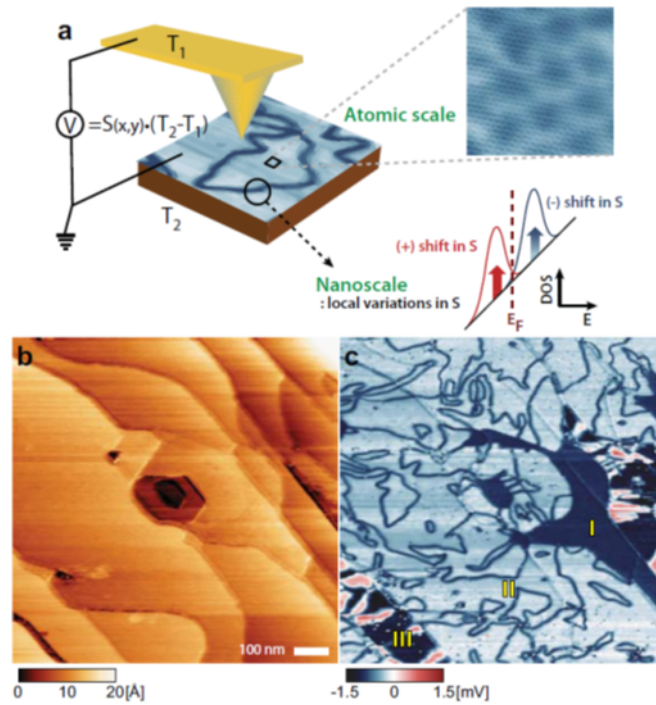


Figure 8. Thermoelectric imaging and its application to an epitaxial graphene. (a) Schematic of a thermopower imaging method. (b) AFM topographic height image and (c) thermopower image simultaneously obtained from epitaxial graphene.

Results and Discussion

a) Thermal rectification using non-linear temperature dependence of thermal conductivity

The goal on this front was to develop and demonstrate a thermal diode, with preferential heat conduction in one direction over the other. It was our intention to show that this can be achieved in designs with a non-linear thermal conductance dependence on temperature and a structural asymmetry. We started with a well-characterized material,

PNIPAM, because of its phase transition at 32°C, where it releases water and changes phase from hydrophilic to hydrophobic. The phase change is expected to lead to a change in the thermal conductivity, with which one could implement the thermal diode concept in a series combination of such a material with another material of nearly constant thermal conductivity. We indeed observed a decrease in effective thermal resistance of our PNIPAM-PDMS structure occurs as a result of phase separation of water from PNIPAM when heated above the lower critical solution temperature (LCST). Above the LCST, convection of water within the PNIPAM compartment becomes possible, creating an additional heat conduction path and thus a decrease in the thermal resistance. The temperature difference between hot and cold sides was measured as a function of input power to the resistive heater and plotted in Figure 9. The forward direction shows an increase in thermal conductance above the phase transition temperature, equivalent to the ‘built-in’ potential in an electronic diode, while the conductance in the reverse direction exhibited only gradual change with temperature.

A simple steady state thermal resistance model was used to predict the behavior of the PNIPAM-PDMS system. The system of equations below is solved numerically for Q and T_1 for known T_o , R_o , and $R_l(T)$ with T_{avg} equal to $(T_o + T_1)/2$.

$$T - T_o = Q \times R_o + (T_1 - T_o)$$

$$(T_1 - T_o) = Q \times R_l(T_{avg})$$

R_l is assumed to have the form of a step function, going from high resistance to low as in the following equation:

$$R_l(T) = a \left(1 - \frac{b}{1 + e^{c(T - T_c)}} \right)$$

Where T_c is the transition temperature ($\approx 32^\circ\text{C}$). The form of R_l is a step function, going from high resistance at low temperature to lower resistance. The form of R_l and the result of the simulation is shown in Figure 10. R_o is the thermal resistance of the PDMS, given by $1/(\kappa L) = 392$ for a PDMS slab of 1.7 cm height. R_l goes from 392 to 100 at high temperature, which is the approximately the thermal resistance of 1.6 cm of water at 0.6 W/(mK).

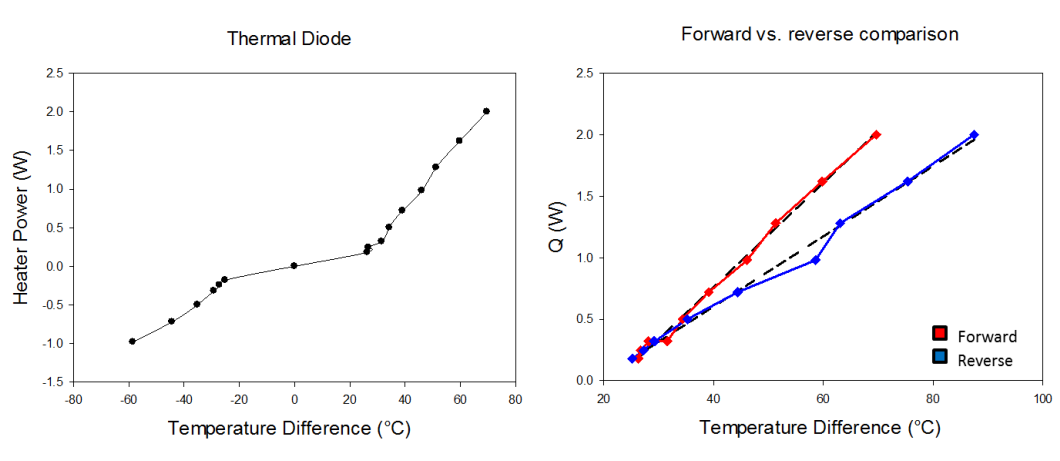


Figure 9. Plot of diode behavior in PNIPAM-PDMS system (left) and comparison (right) of forward (red) and reverse (blue) heat input versus temperature difference ($T - T_o$) from the PNIPAM-PDMS thermal diode.

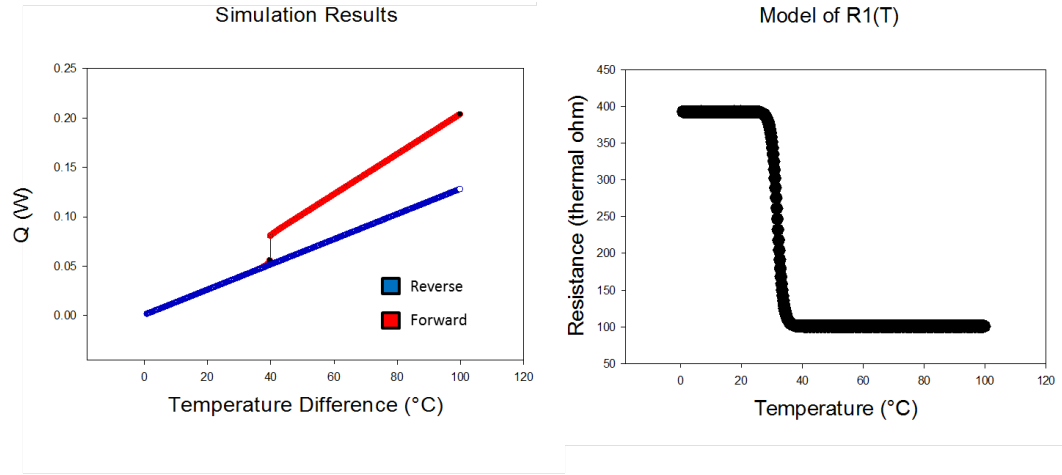


Figure 10. Result of numerical modeling (left) of thermal diode, showing increased conductivity above the phase transition temperature. The temperature dependence of the thermal resistance of PNIPAM (right) is modeled as a step, going down at the phase transition temperature.

The slope of the forward (red) curve above the phase transition temperature is computed as 0.0425 with 0.0015 standard error, while the slope of the reverse curve (blue) is 0.0283 with a standard error of 0.0009. The effective thermal conductivity across the device can be computed as $\kappa_{eff} = hQ/(\Delta T)$, where h is the height of the device, A is the total surface area including the sides, and $Q/\Delta T$ is the slope. In the forward direction $\kappa_{eff} = 0.676$ W/(m·K) above the phase transition, $\kappa_{eff} = 0.345$ W/(m·K) below the transition temperature. The reverse direction is nearly the same as the forward direction below the T_c and is estimated as $\kappa_{eff} = 0.380$ W/(m·K). This gives a rectification ratio of approximately 2 between the forward and reverse modes of operation. It is encouraging that the thermal conductivity of the forward direction is close to that of water (0.6 W/m·K) but it is provocative that the effective thermal conductivity in both directions is higher than the thermal conductivity of PDMS alone. Nevertheless, we have shown that the thermal conductivity change in the forward direction results in an increase in the conductivity across the composite and that this principle can be used in other materials that have a strong temperature dependence of thermal conductivity. A focus of our future efforts along this direction will be in finding solid state materials that have a large temperature dependence on the thermal conductivity and creating a solid state thermal switch or thermal memristor. Further exploration of thermal rectification in other materials with temperature dependent thermal conductivity, such as eicosane based PCMs or solid oxides, deserves additional attention because of the great potential for breakthrough an innovative energy solutions.

b) Self-regulated cooling via synthetic sweating

In this work, experimental results of the temperature response in the self-regulating synthetic sweating structure and numerical simulations to support the results are developed. Experimental results show a sharp rise in temperature initially, until the phase transition temperature of 32 °C is reached and the polymer begins releasing water, and sweating through the membrane. The released water is syphoned to the outer membrane surface via capillary action in the membrane pores. This “sweating” action is accompanied by water evaporation on the membranes outer surface, which completes the heat removal process. This process of capillary-assisted convection and vaporization of the water from the pores has a heat removal capacity that is greater than the heat input. Therefore a long lasting constant temperature plateau develops around the 32°C transition temperature of the enclosed hydrogel.

We model the transient heat transfer characteristic in our composite system by solving

the heat equation for the temperature distribution ($T(x,t)$) with appropriate boundary conditions as shown below. The sweating effect is modeled as a heat flux boundary condition. The heat flux (q_{out}) through the porous membrane consists of a convective contribution as well as a contribution from the latent heat. The latter corresponds to the heat required to evaporate the mass of water that is transported to the membrane surface once the sweating action begins. This term is given by the product of the mass flow rate (m'') and the latent heat of evaporation (L_{evap}). The convective contribution is expressed as the product of the convection heat transfer coefficient, h_c , and the difference between the membrane temperature (T_i) and the external ambient temperature (T_{amb}). The density (ρ) of the hydrogel approximately 1.1 g/cm^3 . Next we will discuss the form of the functions used to model the temperature dependence of the heat capacity, C_p , the thermal conductivity, κ , and the coefficients h_c and m'' in the heat transfer boundary condition, q_{out} . Phase change and flow in porous media are extensive topics beyond the scope of this study, though we can develop intuition about the form and magnitude of the model parameters from textbook equations and the experimental results.

$$(\rho C_p(T)) \frac{\partial T}{\partial t} - \nabla \cdot \left(\kappa(T) \nabla T \right) =$$

$$q_{out} = q_1 + q_2 = h_c (T_i - T_{amb}) + m'' (L_{evap})$$

$$m'' = h_m (\rho_i - \rho_{amb})$$

$$q_{in}(x=0) = Q_o = 0.7 \text{ W/cm}^2$$

$$T(x,0) = T_{amb} = 23^\circ \text{C}$$

The convection heat transfer coefficient, h_c , is assumed negligible below the phase transition temperature because the porous layer insulates the hydrogel surface from the environment. At this point, no water is available to imbibe the pores and they are filled with air. Knudsen diffusion of air through the nanometer scale pores is extremely slow so we model the mixed convection heat transfer coefficient as completely negligible below the phase transition temperature. Once the phase transition begins, water is drawn into the pores by capillary action and the convection coefficient should rise at least to the that of free convection of water, which is typically $20\text{-}100 \text{ W/(m}^2\text{K)}$. This coefficient can be much higher if forced convection by air blowing over the composite, up to $10,000 \text{ W/(m}^2\text{K)}$, but we assume it at least reaches the upper bound of free convection ($0.01 \text{ W/cm}^2\text{K}$).

The mass flow rate, m'' , is also considered negligible below the transition temperature, because water is bound by the polymer matrix, but when the hydrophilic to hydrophobic transition occurs and water is expelled and taken into the pores, it is allowed to vaporize upon arriving at the top surface, removing heat at the rate of mass flow times the latent heat. m'' is equal to the mass transfer coefficient, h_m , times $(\rho_i - \rho_{amb})$, the difference in vapor density between the ambient and the interface. The mass flow rate is difficult to determine exactly, but can be estimated from our experimental results. In Figure 12, we see that the flat portion of the curve lasted for approximately 2 hours until complete dry-out occurred. With our starting $250 \text{ }\mu\text{L}$ of water, a simple estimate of the mass flow rate gives approximately 0.001875 mL/min . This gives the vaporization heat flux, $q_2=4.18 \text{ J/min}$, or about 70mW . We note that this corresponds to 10% of the input power supplied to the resistive heater. Including this figure into the boundary condition produced a long lasting constant temperature plateau, similar to that observed in our experiment. The results of the simulation are shown in Figure 11.

The vapor density difference is the parameter that cannot easily be measured but there is

a relationship between the vapor density at the interface and the pore size that can tell us about the vaporization rate. The Kelvin equation describes the change in vapor pressure due to a curved liquid vapor interface with radius r . Upon initial wetting, the water in the pores forms a meniscus with radius of curvature on the order of the pore size, and the vapor pressure, p_i , at the meniscus can be related to the radius of the pore as follows:

$$\ln \frac{p_i}{p_o} = \frac{2\gamma V_m}{rRT}$$

showing that higher mass transport rates are achievable with decreased pore size as a result of the higher saturated vapor density (or pressure) achievable around interfaces with smaller radius of curvature. The pore radius now becomes an important parameter in the figure of merit of the composite when the mass transfer rate becomes the limiting factor in heat removal. The exact size of the pores to achieve noticeable changes in the mass transfer rate is not obvious at this point, but a plot of the saturated vapor pressure versus pore radius, using the molar volume, V_m , and surface tension, γ , properties of water, shows that this effect only becomes significant when pore sizes reach the sub-100 nm range (Figure. 13).

The heat capacity also plays a significant role in the transient heat characteristic because the heat rise is inversely proportional to the mass times the heat capacity at temperatures below the transition, as the heat flow out of the composite is small before the phase transition. Measurements taken from Tiktupulo *et al.* are used as a model for the specific heat, showing a Gaussian peak about 5.5 times of the height of the specific heat below the transition. The total heat capacity of the composite can be taken as the sum of its parts. Considering that PNIPAM absorbs approximately ten times of its weight in water, we can write the total specific heat capacity of the composite as follows:

$$C_{p,tot} = m_{tot} (0.1 \times c_{p,PNIPAM} + 0.9 \times c_{p,H_2O})$$

which is also plotted in the figure below beside the figure from Ptistyn *et al.* for comparison.

A combined Gaussian function and step function was used for $C(T)$ to model the data from Ptistyn which follows the equation:

$$C_{p,PNIPAM}(T) = 4.5e^{-\frac{(T-32)^2}{\sigma^2}} + 1 - \frac{1}{2(1 + e^{-(T-32)})}$$

A plot of the model heat capacity is shown in Figure 14. The heat rise in our simulation results is faster than in the experimental results, but this can be attributed to the added thermal mass of the device and parasitic heat paths in the device, such as through the sidewalls, which had a thermal conductivity of only 4x less than the composite, which is still significant. The simulation assumed the heat flux was applied directly and instantaneously to the composite. In real applications these things must be considered and will be incorporated in future modeling and experimental efforts.

To summarize, we have developed a model that recreates the behavior of our experimental self-regulated cooling structure. The self-regulated synthetic sweating mechanism may find its uses in applications where power consumption is tied to thermal control, and in distributed engine self-lubrication, fuel cell supply and water removal, and drug delivery or biofluid sample extraction.

Another application that has garnered some interest is the cooling of data centers. A large portion of the US energy budget is attributed to data centers and the need for effective rack-level power and cooling monitoring and dynamic management capabilities are needed, according to a 2008 Intel press release [17]. A self-regulated thermal management solution, demonstrated in our efforts, has the advantage of being most efficient and on-demand. It could be of interest to the data center operators and will be pursued in the coming months. A provisional patent has been filed on this technology and interest for commercial use will be gauged in the near future.

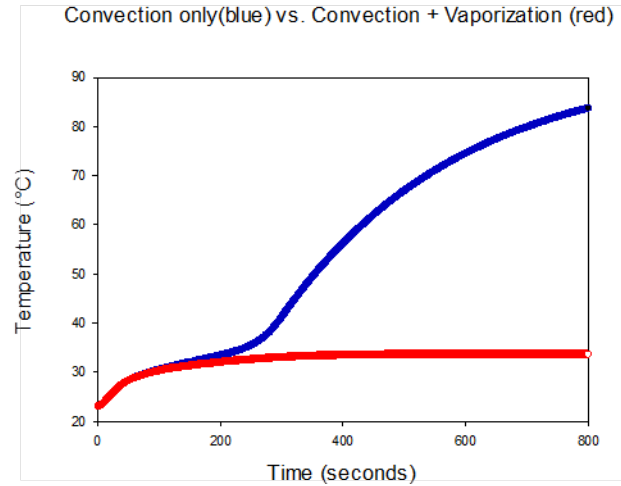


Figure 11. Comparison of convection only (blue) and convection with mass flow boundary conditions (red) for heat removal at the composite interface. The initial conditions are chosen to match the experimental settings. The additional heat removal from vaporization of water results in a long lasting constant temperature plateau, as seen in the experimental results.

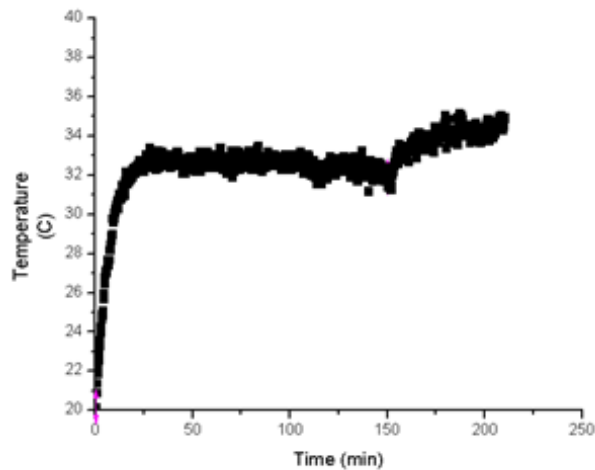


Figure 12. Demonstration of synthetic skin. Fast initial temperature rise due to small thermal mass. After reaching the phase transition temperature of the PNIPAM hydrogel, a long constant temperature plateau representing latent heat storage and fast evaporative cooling defines the device.

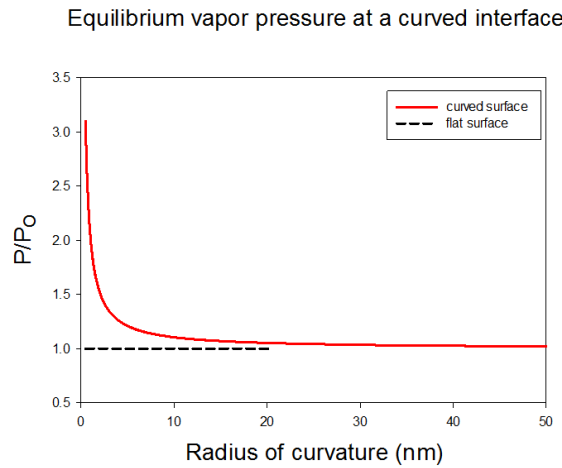


Figure 13. Plot of saturation vapor pressure, or escape tendency, for a curved surface of radius r . Below 100 nm pore size, increase in mass flow rate becomes dominant.

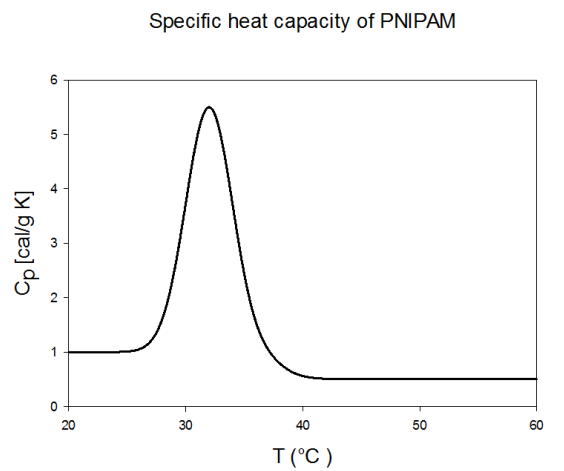


Figure 14. Heat capacity of hydrogel composite showing a peak around the transition temperature, modeled after data in Figure 3(a) of Tiktópulo *et al.*

c) Electrical and thermal transport behavior of nanostructures fabricated by AIPEL (Atomic Image Projection E-beam Lithography)

This part of the project aims to fabricate nanostructures with various dimensions and morphologies by fine-tuned AIPEL system, installed and operated by KPI's laboratory (Prof. Ki-Bum Kim at SNU), and to characterize the electrical and thermal transport behavior of the fabricated nanostructures. Nanostructures, such as nanowires and nanotubes, have gathered great interests as a future thermoelectric platform by decoupling electron and phonon transport and thereby improving thermoelectric figure of merit. Over conventional e-beam lithography and synthetic methods, AIPEL system has many advantages to fabricate nanostructures. Since AIPEL uses naturally existing materials as a mask for e-beam lithography, the nanoscale periodic patterns can be formed on a large surface area ($> 100 \mu\text{m}^2$) substrate only for a very short time. In addition, non-straightforward nanostructures, such as nanoflowers and corrugated wires, can be readily patterned by introducing various masks. By exploiting these merits, we have performed the fabrication of various nanostructures by the AIPEL system and investigated the electron / phonon transport behavior through those.

For the establishment of the AIPEL process, Si, one of the most widely used materials for IC chips and thermoelectrics, has been chosen firstly and tested. Figure 15 shows one

example of AIPEL-patterned corrugated Si nanowires by applying β -Si₃N₄ mask and optimizing e-beam dose. For the dose of 700 $\mu\text{C}/\text{cm}^2$, very clear and well-defined corrugated surface can be formed on the Si nanowires, of which the detailed dimensions are specified within the figure. Not limited to the corrugated structure, other morphologies of nanostructures can be fabricated by rigorously selecting the mask material, as demonstrated in our previous publications [5,6]. Furthermore, the dimension (pitch and width) and target materials have a wide range of choices with the control of process parameters (dose, magnification, etc.) and with the selection of substrates. This achievement can open a door to investigate the electrical and thermal transport behavior of chalcogenide materials which are the most widely studied materials for the thermoelectrics.

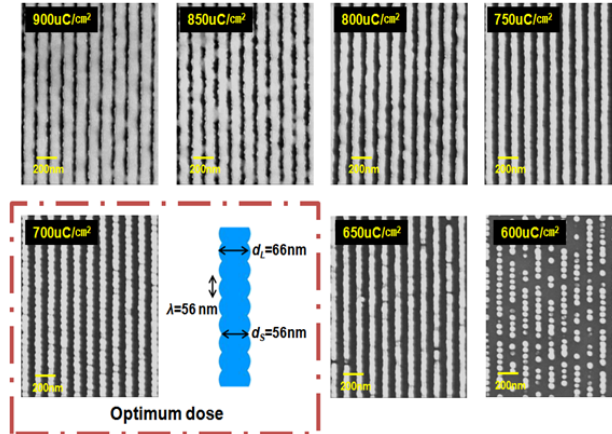


Figure 15. SEM images of AIPEL-patterned corrugated Si nanowires with various e-beam dose. The magnification was fixed to 200 and high-resolution TEM image of β -Si₃N₄ was used as a mask.

Motivated by the successful development of AIPEL process, the fabrication and characterization of Bi nanowires were pursued. The Bi nanowires have gathered a great interest as thermoelectric materials owing to its semi-metallic property and extraordinary thermoelectric power and therefore it is thought to be one of the suitable materials in this project. Prior to the nano-patterning process, our team had to set up a deposition method of conformal Bi films in order to guarantee smooth surface of fabricated nanowires. Since Bi has a relatively low melting temperature and high thermal expansion coefficient, either hillocks formation or agglomeration was observed during sputtering and thermal evaporation of Bi films. These rough surfaces indeed resulted in much higher (1-order-of-magnitude) film resistivity compared to the bulk material. In order to obtain high quality Bi films, PLD was introduced and various parameters, including target-substrate (TS) distance, working pressure, and substrate temperature, were optimized. Figure 16 illustrates our efforts on optimizing (or minimizing) the electrical resistivity of PLD-Bi films. It is surprising and counter-intuitive that the electrical resistivity became lower and lower as the deposition rate increased. In addition, the films deposited by higher deposition rates have much smoother surface. This indicates that the high deposition rate resulted in the decrease of effective surface diffusion length of Bi monomers and thereby the formation of hillocks was kinetically inhibited and the surface scattering of transporting electrons was successfully suppressed. Upon the optimization, it should be noted that the PLD-Bi films showed very rough root-mean-square roughness of 1.57 nm (as-deposited) and 1.29 nm (post-annealed), which are more than 1-order lower than the thermal evaporated film (24.2 nm), as shown in the AFM images in Figure 17. In addition, the electrical resistivity of PLD-Bi films was as low as 300 $\mu\Omega\text{ cm}$ which ensures enough high electrical conductivity beneficial for a high ZT value. Our findings on ultrasmooth and ultraconductive Bi films would generate great interests and impact on the thermoelectric research field that has suffered from its lack of materials platform.

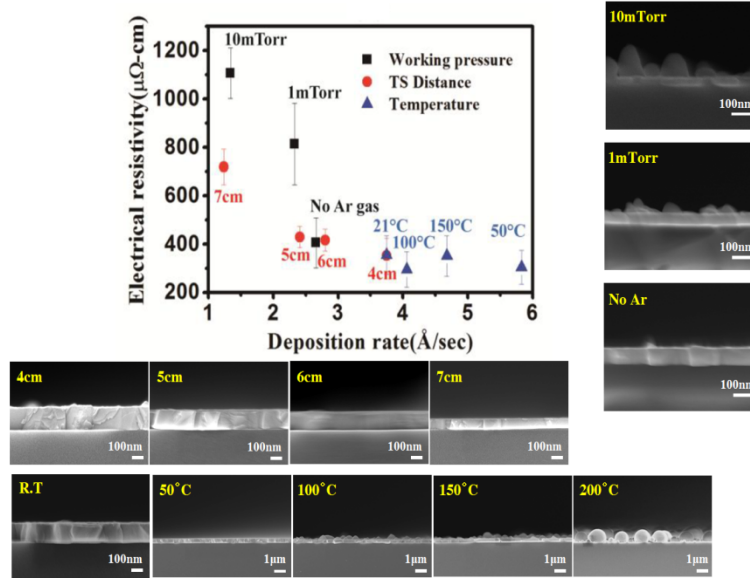


Figure 16. Electrical resistivity of PLD-Bi films as a function of film deposition rate. SEM images show cross-sectional view of Bi films deposited with various TS distances, substrate temperatures, and working pressures.

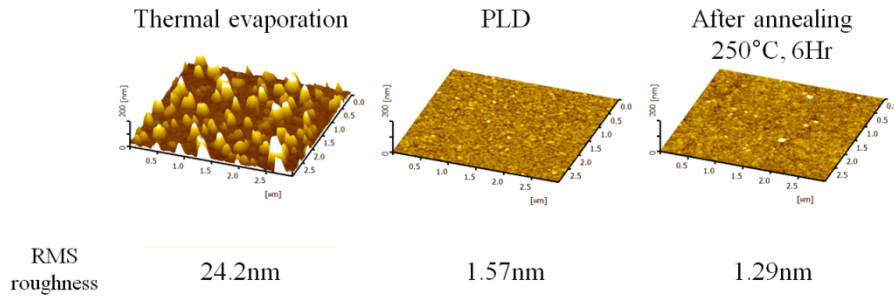


Figure 17. AFM images of Bi films deposited by thermal evaporation (left) and PLD (center for as-deposited and right for post-annealed). RMS roughness of each film is marked below the images.

The ultrasmooth PLD-Bi films were subsequently nanopatterned by the AIPEL system. 50-nm-thick Bi films was deposited onto SiO_2 (100nm) / Si substrates and was patterned into nanowires as schematically shown in the experimental section. Upon variation of e-beam dose from 850 to 1000 $\mu\text{C}/\text{cm}^2$, our team could obtain the fine-tuned Bi nanowires with various widths ranged to 55 - 80 nm (Figure 18). On the fabricated Bi nanowires, Ti/Au electrodes were formed by e-gun evaporation and lift-off process at the both ends of nanowires. You may find the schematic, optical, and SEM images of fabricated devices in Figure 19. By exploiting this platform, we aimed to investigate electron transport behavior through Bi nanowires. Specifically, temperature-dependent electrical resistivity of Bi nanowires was studied by obtaining I-V characteristics [Figure 20(a)]. Figure 20(b) shows the electrical resistance of Bi nanowires as a function of measurement temperature. Herein, the resistance indicates the reciprocal of a slope of I-V curves in (a). Interestingly the resistance initially decreased with increasing the temperature and then it increased above 70 °C. This result might indicate that the fabricated Bi nanowires exhibit metal-to-semimetal transition at that temperature. In order to understand this behavior, the electrical resistivities of various forms (bulk, thin film, and nanowires) of Bi were compared in Figure 21. The electrical resistivity of Bi nanowires was relatively higher than the thin film and bulk. This result suggests that the confinement effect of nanowires affect the electron transport. So as to the electrical conductivity, we may imagine that the phonon confinement in this structure would be more dominant, owing to its

much longer mean free path, and would result in a drastic decrease of thermal conductivity. It is obvious that the metal-to-semimetal transition behavior is only obtainable in the nanowires case. At this point, an origin of this interesting and extraordinary phenomenon is still unclear. However, one of the big differences between nanowires and thin films is the activation energy for the electron transport. As shown in Figure 21(b), the Bi nanowires have a steeper slope compared to the film and this indicates that the nanowires have much higher activation energy (15 meV) than the thin film (2 meV). An origin of this deviation is under consideration and need more study to clarify that. Based on the formation of Bi nanowires and the characterization of electrical properties, investigation of thermal transport properties and thermoelectric power of Bi nanowires will be performed, upon developing measurement method and system, as a follow on the project. Once the Bi nanowires are proven to have the highest ZT value (>2), the findings in this work will bring about renewed interests and perhaps a new paradigm in thermoelectric material fabrication.

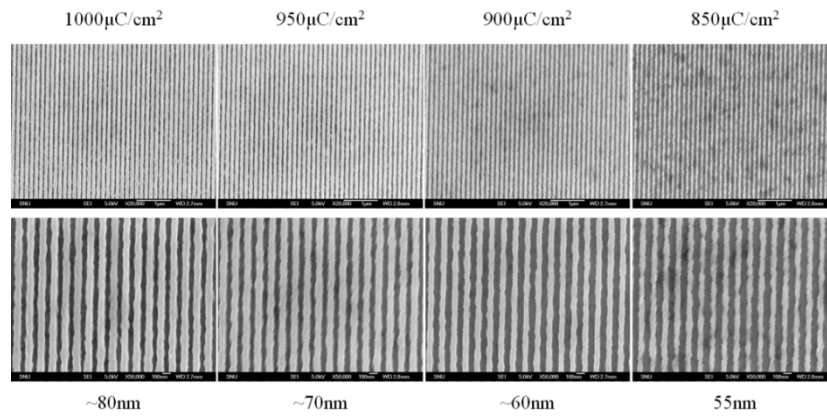


Figure 18. SEM images of Bi nanowires fabricated by AIPEL system with variation of e-beam dose.

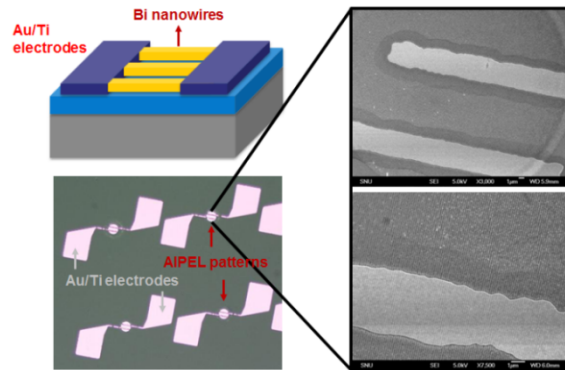


Figure 19. Schematic (top-left), optical (bottom-left), and SEM (right) images of Bi nanowires devices for measurement of electrical properties.

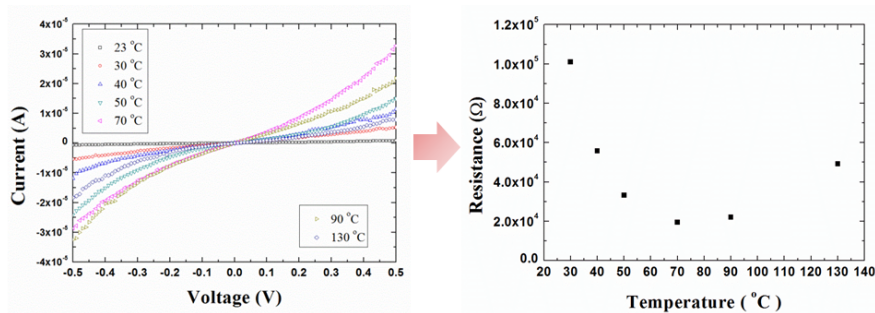


Figure 20. (a) I-V characteristics and (b) resistance of Bi nanowires with respect to

measurement temperature.

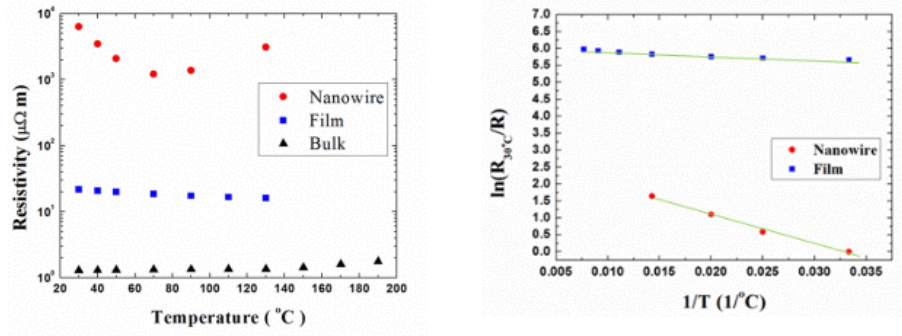


Figure 21. (a) Temperature-dependent electrical resistivities of Bi nanowires, thin film, and bulk. (b) $\ln(R_{300C}/R)$ versus a reciprocal temperature.

d) Thermoelectric power enhancement via AAO-templated nano-patterning

This effort has focused on improving thermoelectric power (or Seebeck coefficient, S) of materials via novel nanopatterning. As well described in the definition of ZT value ($=S^2\sigma T/\kappa$ where σ and κ are electrical and thermal conductivity, respectively), one may expect to increase the thermoelectric figure of merit by increasing S and σ or decreasing κ . In order to improve ZT , most efforts have been given to decouple electron and phonon transport; i.e. decreasing a thermal conductivity while maintaining an electrical conductivity by using either nanopatterning or superlattice structure. However, there have been almost no efforts on improving the thermoelectric power even though it has much dominant effect from its definition. In this project, our team aims to improve the thermoelectric power of Bi and carbon nanotube (CNT) films via novel AAO-templated nanopatterning which results in a unique nanomesh structure. It should be emphasized that this research work has been closely collaborating between USPI's and KPI's groups; a student (Seungwoo Jung) of KPI's group had participated in USPI's group (Brown University) for 6 months and mainly performed the experiments.

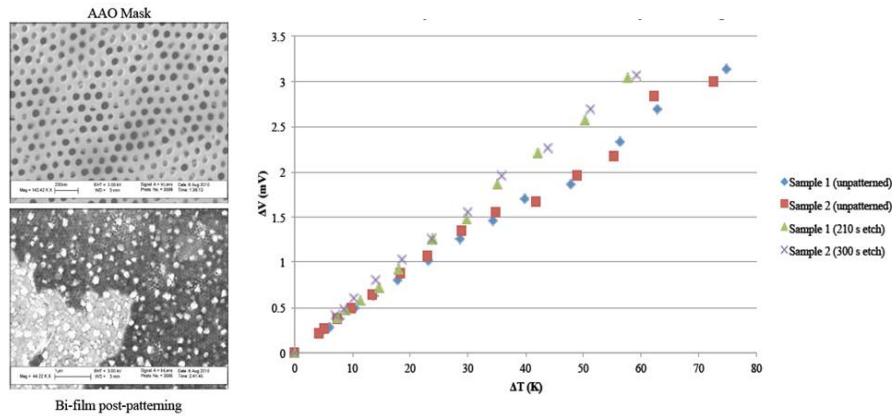


Figure 22. SEM images of highly periodic AAO mask (top-left) and nanomesh-patterned Bi film (bottom-left). Thermovoltages of the prepared samples as a function of temperature difference (right).

A preliminary effort has given to the formation of Bi nanomesh structure and characterization of thermoelectric power. Detailed process and the measurement system can be found in the experimental section. Figure 22 shows the plan-view SEM image of nanopatterned Bi film and the measured thermovoltages as a function of temperature difference. As well replicated the highly ordered nanoporous AAO template, the nanopatterned Bi film

had a fine-tuned nanomesh structure. It is interesting that the thermoelectric power of Bi film increased about ~24 % by nanopatterning compared to the pristine film. Further investigation on electron and phonon transport behaviors would reveal the impact of nanomesh patterning on improving the thermoelectric figure of merit. If proven to be successful, this method would be the easiest, fastest, and large area appropriate one which can be applied to any target material.

Our efforts have been extended to the CNT film which has been considered to have near-zero Seebeck coefficient. As same as the case of Bi nanomesh, the nanoporous AAO template was used as a hard mask for RIE of CNT films. Figure 23 shows the SEM images of (a) pristine CNT and (b) nanomesh-patterned CNT films. CNT itself has a nanomesh structure but the nanopatterning added highly periodic, reproducible and large-area-controllable nanomesh structure atop of that. The nanopattern had 100-nm period and 50nm pores. On these pristine and nanomesh CNT films, thermoelectric power values were measured using the apparatus introduced in the experimental section. Figure 24 shows the thermovoltages across hot and cold ends as a function of temperature difference. It is clear that the nanomesh CNT film has much larger slope than the pristine one. Estimated Seebeck coefficients were 29.5 $\mu\text{V/K}$ and 39.5 $\mu\text{V/K}$ for the pristine and nanomesh CNT films, respectively. Surprisingly, this result suggests that the thermoelectric power of CNT film can be also enhanced (~34 %) by the AAO-templated nanopatterning, as same as the case of Bi film.

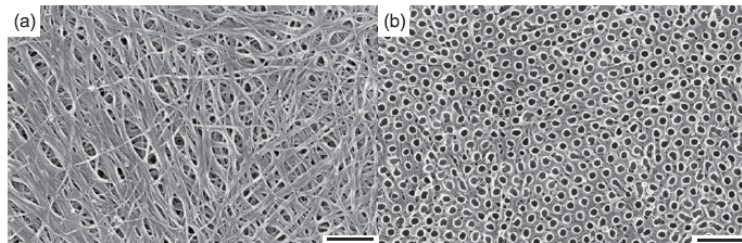


Figure 23. SEM images of (a) pristine and (b) nanomesh CNT films. Scale bar indicates 300 nm.

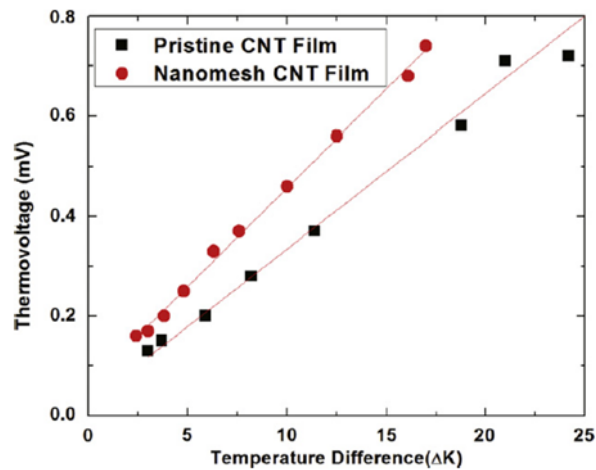


Figure 24. Thermovoltages of pristine and nanomesh CNT films as a function of temperature difference.

In order to understand the origin of the enhanced thermoelectric power, Raman spectra [Figure 25(a)], UV-Vis-NIR absorption spectra [Figure 25(b)], and temperature-dependent resistance [Figure 26] were obtained. As shown in Figure 25(a), the Raman G to D peak ratio drastically decreased from 39 (pristine) to 14 (nanomesh) via nanopatterning. This result indicates that the nanomesh film holds damaged sp^2 bonds. This aspect can be also found from the reduced peak areas correspond to S33, S22, and M11 transitions in the case of the nanomesh CNT film [Figure 25(b)]. In addition, the absorption spectra indicate that the CNT

films used in this study have both metallic and semiconducting CNTs. Figure 26 shows the temperature-dependent electrical resistance of pristine and nanomesh CNT films. The electrical conduction is expected to occur by variable range hopping (VRH) conduction as the resistance curve can be described as $R(T)=R_0\exp[-(T_0/T)^{1/4}]$. Such plots, energy barrier for the electron hopping could be extracted from those slopes. For the low temperature regime (inset figure, 80-250K), both pristine and nanomesh films exhibit the semiconducting behavior but the energy barrier of nanomesh film (39.3 meV) was much higher than the pristine film (1.15 meV). Meanwhile, at high temperature regime above 250 K (main plot in Figure 26), two films have opposite signs of slopes and thereby one may conclude that the nanomesh film is still semiconducting while the pristine one changed to metallic. In addition, the energy barrier of nanomesh film greatly increased to 0.95 eV. These results might suggest that some of mobile π electrons are localized at the defect sites (i.e. broken sp^2 bonds and oxygen termination) formed the nanopatterning and this localization might be responsible for both the semiconducting behavior and substantially increased Seebeck coefficient of nanomesh CNT film. The results on the nanomesh-patterning of CNT films and the related characterization of thermoelectric power and optical / electrical measurements were published in Nanotechnology, 23, 135704 (2012) [18] and it was achieved based on the close collaboration between USPI's and KPI's research groups. Our findings would bring about great attention from the researchers working on the thermoelectrics since those suggested a possibility of thermoelectric power control by the simple, cheap, fast, and large-area nanopatterning process.

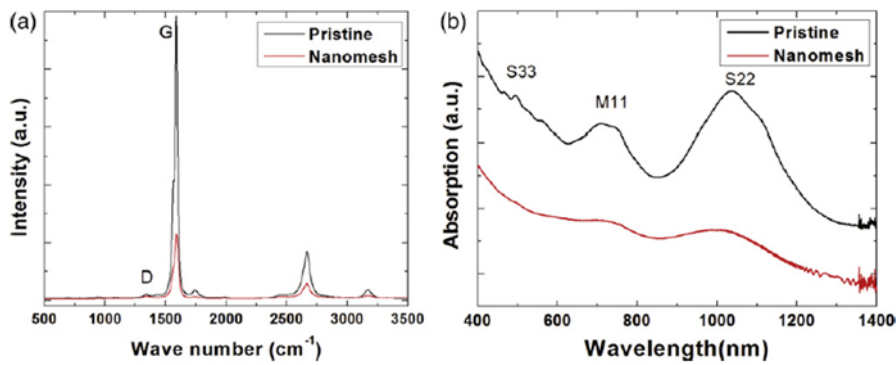


Figure 25. (a) Raman spectra and (b) UV-Vis-NIR absorption spectra of pristine and nanomesh CNT films.

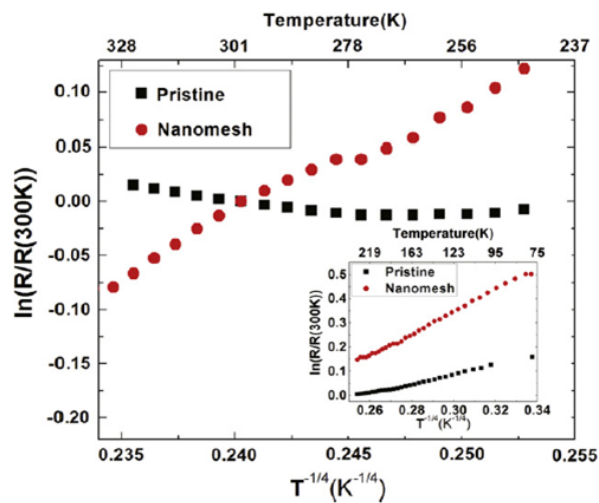


Figure 26. Temperature-dependent resistance curves of pristine and nanomesh CNT films. Inset plot shows the curve obtained at a low temperature regime (80-250 K).

e) Heterolayered Al-doped ZnO composites as transparent thermoelectrics

The objective of this work is to establish a new platform of “transparent thermoelectrics” with combinatorial use of transparent conducting oxide (TCO) materials and heterolayered doping in atomic layer deposition (ALD). The development of ALD-grown TCO materials was started by KPI’s group concerning an investigation of electron transport behavior and charge generation mechanism of Al-doped ZnO (AZO) as a replacement of the most popular indium-tin-oxide (ITO) [14,15]. The precedent studies performed by KPI’s group have mostly focused on structural and electrical characterization of ALD-AZO films. Introduction of scanning electron transmission microscopy-high angle annular dark field (STEM-HAADF) revealed that the ALD-AZO has a unique heterolayered structure consisted of a ZnO matrix and AlO_x atomic-doping layers, as shown in Figure 27. Even with its layered structure, this film exhibited resistivity as low as $2 \times 10^{-3} \text{ cm}$ owing to its extremely high electron concentration of $3 \times 10^{20} \text{ cm}^{-3}$ (Figure 28). Motivated by these findings, we have turned to investigate UV-visible / infrared (IR) / microwave optics and thermoelectric properties of this system. Since oxide materials have extreme thermal stability and nontoxicity and the ALD process guarantees extremely conformal deposition of films onto arbitrary substrate at a low temperature, the combination of these two merits has lead us to establish a platform for the transparent thermoelectrics with the heterolayered AZO composites. This project has been closely collaborated between KPI’s (ALD process / electrical properties / UV-Vis optics), USPI’s (IR / microwave optics), and Co-PI’s (thermoelectric properties) groups.

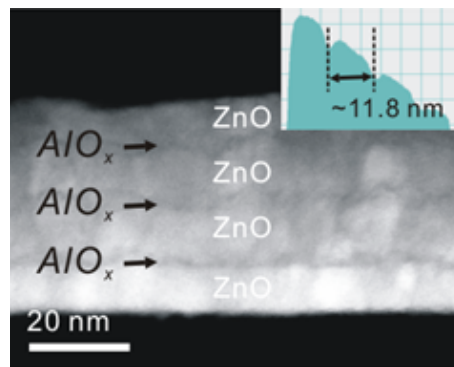


Figure 27. Cross-sectional view STEM-HAADF image of ALD-AZO film. An ALD cycle ratio was ZnO 49 : AlO_x 1.

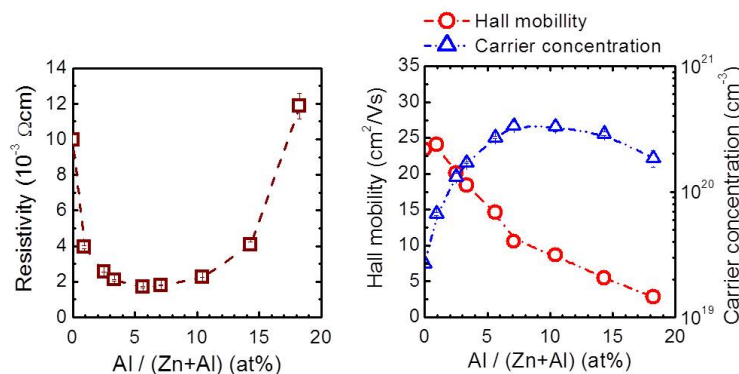


Figure 28. Electrical resistivity, Hall mobility and carrier concentration of ALD-grown heterolayered AZO films as a function of Al cation ratio $[\text{Al}/(\text{Zn}+\text{Al})]$.

Optical characterization of heterolayered AZO has been performed in the three separate regime of UV-visible, IR, and microwave (THz) regime. AZO has a wide optical bandgap ($>3.0 \text{ eV}$) and thereby is optically transparent to the visible light. In contrast, the extremely high density of free electrons and oscillation of those makes this material to be highly

reflective to the IR and microwaves. Specifically this cut-off frequency (ω_p , plasma frequency) is defined as proportional to square root of electron density (n) [$\omega_p = (ne^2/\epsilon_0\epsilon_r m^*)^{1/2}$]. Firstly, UV-Vis transmittance was measured for the various doping concentrations of AZO films deposited on a quartz substrate with a thickness of 150 nm. As shown in Figure 29, the AZO films exhibited high transmittance over 90 % for the overall visible light range, which is attributed to the large optical bandgap and low absorption coefficient. Herein, it should be noted that the transmittance, especially in 400-550nm range, gradually increased with increasing the doping concentration. This is opposite to the conventional TCO materials which show increased free electron scattering/absorption and result in decreased transparency. For instance, we doubt this counter-intuitive observation attributed from both the reduced reflection due to the free electron shielding and enhanced film crystallinity. Another thing to be considered is that, as increasing the doping concentration, the transmittance curve continuously blue-shifted. Typically this blue shift (Burstein-Moss shift) has been known to occur by the conduction band filling of free electrons. However, in the heterolayered AZO, it is observable that this blue-shift continued even if the release of free electrons was retarded at high doping concentrations, as in Figure 29. Such a decoupling of the optical bandgap and free electron density is not the only parameter explaining the optical bandgap widening of this system. For instance, we investigated lattice parameter evolution with changing the doping concentration and found that both [10-10] and [0002] direction lattice parameters were gradually reduced by the atomic-layers doping [Figure 30]. This result might indicate that each atomic-doping layer induced a strain in the ZnO lattice and this strain would be responsible for the unconventional optical bandgap widening of ALD-AZO composite. Modified band structures of this material were suggested in Figure 30. Our findings would give a great impact on the semiconductor society by providing a new methodology of controlling optical bandgap of materials via the atomic-layers doping.

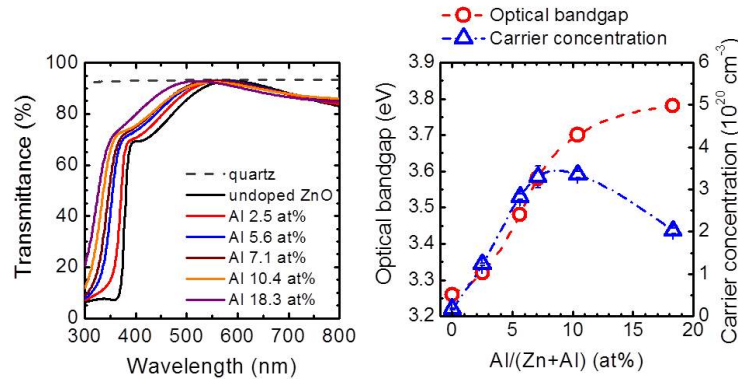


Figure 29. UV-Vis transmittance curve (left), optical bandgap and carrier concentration (right) of heterolayered AZO films with respect to a doping concentration (Al cation ratio).

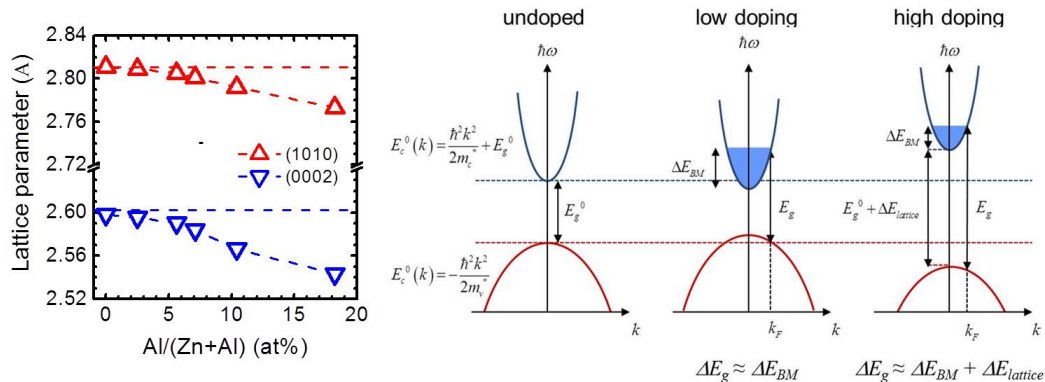


Figure 30. Lattice parameters extracted from XRD patterns (left) and proposed band

structures of ALD-AZO composites. For a low doping concentration, the bandgap is determined by the BM shift. In contrast, for a high doping concentration, the widening due to an atomic-layers-induced strain is dominant.

Exploration of the optical properties has been extended to the IR and microwaves regime. As expected from its high electron density, the heterolayered AZO composite has a great potential to be used as a transparent heat mirror (or energy-saving window) and EMI (electromagnetic interference)-shielding windows. The former is beneficial for the thermoelectrics applications and the latter is for the emerging transparent electronics which conventional metal shielding cannot be integrated. Firstly the IR transmission was measured for the same samples using FT-IR system. Figure 31 shows near- and mid-IR transmission of ALD-AZO films with four different doping concentrations (including the undoped ZnO). Contrary to the bare quartz and undoped ZnO, the AZO films exhibited low IR transmission in the NIR regime. By fitting the experimental curves with the Drude model, it was found that this low transmission is mainly due to the high IR reflectivity ($>20\%$). In Figure 31, the IR transmission becomes lower as increasing the doping concentration and thereby increasing the electron density. From the fitting parameters, real (ϵ_1) and imaginary (ϵ_2) parts of the permittivity of ALD-AZO films were extracted in Figure 32. The cut-off wavelengths, which exhibit zero ϵ_1 , were between $3.5\text{--}3.9\ \mu\text{m}$. In this range, its optical loss, ϵ_2 , was very low below 5. This is much lower than conventional Au and Ag (>10), and even lower than metal nitrides (>20) in the similar wavelengths regime. [19-21]. The plasmonic reflection behavior was also investigated in the microwaves or terahertz (THz) regime. In order to measure the EMI shielding efficiency (SE), homemade coax cable was connected to a vector network analyzer. The complex reflectivity of microwaves was measured first and that was sequentially converted into the microwave transmission and SE. Figure 33 shows the EMI shielding efficiency of heterolayered AZO composites in the wide range of $1\text{--}30\ \text{THz}$. It is surprising that the SE is even higher than $20\ \text{dB}$. This indicates more than 99% of EMI signals were effectively blocked by only 150-nm -thick transparent oxides. And those high shielding efficiencies were mostly come from the reflection ($>99\%$) rather than the absorption. These results consistently suggest that our heterolayered AZO composites have a great potential as a low loss plasmonic metamaterials. In practical point of view, these thin coating can be made on arbitrary substrates at a low temperature and work as an effective transparent heat mirror and EMI-shielding windows. The contents of this work have been published in J. Mater. Sci. 48, 2536 (2013) [22].

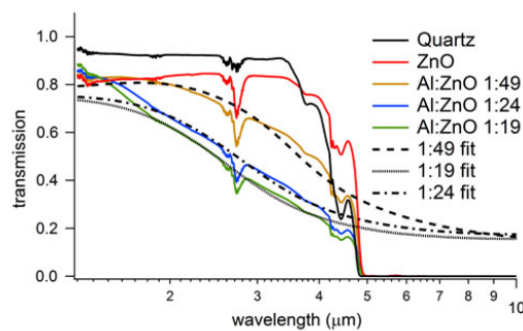


Figure 31. IR transmission of heterolayered AZO samples. Data for the undoped ZnO and AZO films are normalized to that of the quartz substrate. Numbers of the samples denote the ALD cycle ratio of AlO_x to ZnO. Also shown are fits to the Drude model.

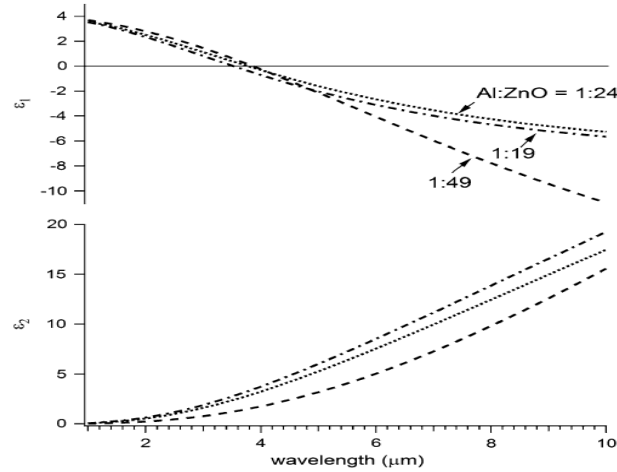


Figure 32. Real (ϵ_1) and imaginary (ϵ_2) parts of the IR permittivity of AZO films extracted from the Drude model fits.

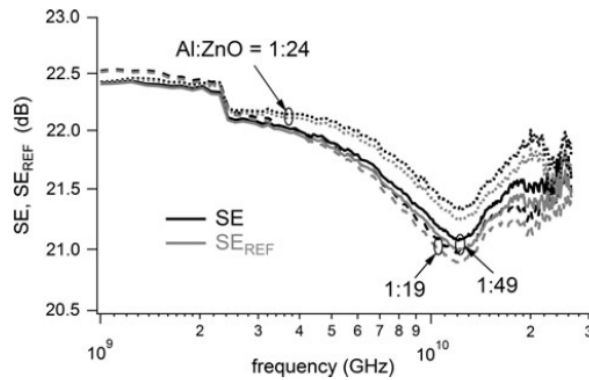


Figure 33. Microwave shielding efficiencies of ALD-AZO composites. The black lines correspond to the total shielding efficiency and the gray lines correspond to the reflective component.

Finally, the phonon transport behavior of ALD-AZO composites was investigated. Relatively thick films (300-500nm) were deposited onto SiO₂ (285nm) / Si wafers by KPI's laboratory and the thermal conductivities were measured by TDTR setup in Co-PI's laboratory (Dr. Lyeo at KRISS, Korea). As shown in Figure 28, the atomic-doping layers successfully released free electrons of $3 \times 10^{20} \text{ cm}^{-3}$ into the ZnO matrix. Therefore the electrical conductivity could increase up to 1,000 S/cm or higher by the doping. In contrast, since the incorporated atomic-doping layers would work as scattering centers for the phonon transport, it is expected that the thermal conductivity would greatly decrease by the heterolayered doping. If this is proven to be valid, then the heterolayered AZO composites can have enhanced ZT values as from its definition, $S^2\sigma T/\kappa$. Figure 34 shows the electrical conductivities and thermal conductivities of ALD-AZO films with various doping concentrations. As expected, the electrical conductivity increased more than one-order of magnitude. In contrast, the thermal conductivity drastically decreased from 15 W/mK (undoped) to below 4 W/mK (7.1 at% Al-doped). These results indicate that the incorporated dopant layers worked as dopants for electrical conductivity, by releasing free electrons, while those layers worked as interfacial thermal boundaries. By considering effect of released free electrons to the thermal conductance, the interfacial thermal conductance at a ZnO/AlO_x interface (G_{true}) was estimated in Figure 34. Interestingly each ZnO/AlO_x interface had the constant interfacial thermal conductance of 1130 MW/m²K. This result suggests a controllability of thermal conductivity by adjusting the density of inserted atomic-doping layers. For these samples, temperature-dependent electrical and thermal conductivities, Seebeck coefficients and figure of merit (ZT) values were obtained in Figure 35. The electrical conductivities slightly decreased as increasing the temperature and this means that all ZnO and AZO films in this study exhibit metallic behavior. In contrast,

the Seebeck coefficient gradually increased to the negative values as increasing the temperature. This behavior is well matched to the well-known Mott-Jones relation. Even though the atomic-layers doping worked positively in enhancing ZT value in terms of electrical and thermal conductivities, the Seebeck coefficient decreased with increasing the doping concentration owing to the released free electrons. Other effects such as effective mass change need to be further studied to clearly understand the temperature-dependent and doping-concentration-dependent change of Seebeck coefficient. Finally the ZT values of undoped and AZO (5.6 at% Al-doped) films were obtained in Figure 35. Aided by its high electrical conductivity and low thermal conductivity, the ZT value of AZO film was slightly higher by 0.002 at 130°C than that of undoped ZnO film. Further engineering, including post-annealing, introduction of other dopants or materials, and heterostructure control, would be required to enhance both Seebeck coefficient and figure of merit of this system. Conjunction with other advantages of optical transparency, heat-conserving, and microwave-shielding properties, continuous efforts and interests should be given to open a door to a new field of “transparent thermoelectrics”.

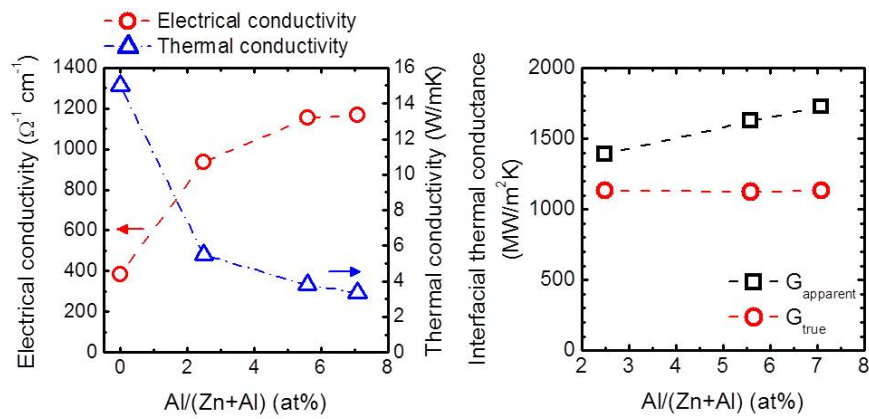


Figure 34. Electrical and thermal conductivities of ALD-AZO composites (left). Interfacial thermal conductance, G_{true} , of each ZnO/ AlO_x interface (right)

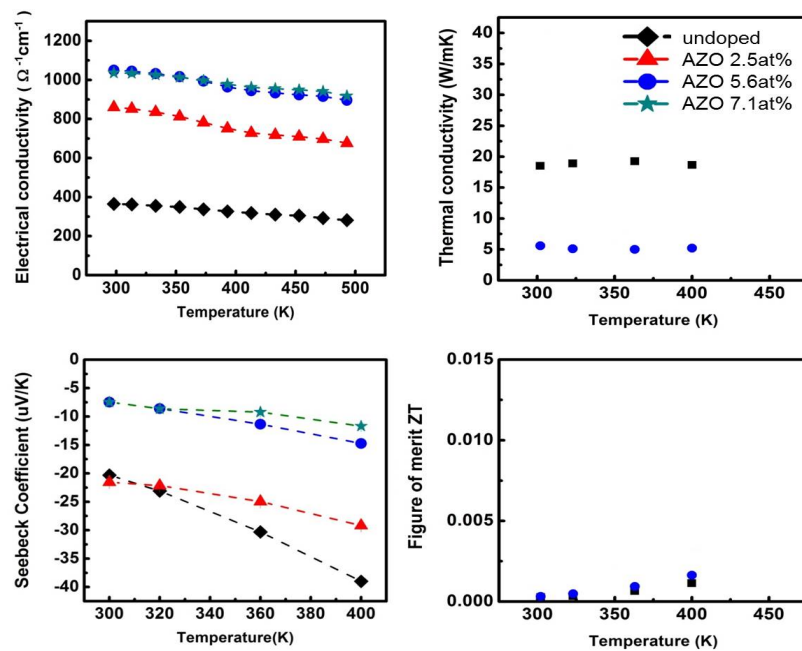


Figure 35. Electrical conductivity, thermal conductivity, Seebeck coefficient, and figure of merit (ZT) of ALD-AZO composites as a function of measurement temperature.

f) Thermoelectric imaging of structural disorder in epitaxial graphene

Finally, we report on a new breakthrough: thermal-voltage imaging of unprecedented atomic resolution and exceeding classical limits. It is a breakthrough, that was neither anticipated nor in the plan at the start, but was propelled by growing interests arising from this effort. Its impact will likely extend beyond thermal management into basic sciences for years to come.

Co-PI, Dr. Lyeo, championed the effort that led to the breakthrough. It is a pursuit of using the thermal properties as tools for microscopic investigation of materials. The results demonstrate the feasibility of observing the local density of states by using the thermoelectric power down to atomically varying details.

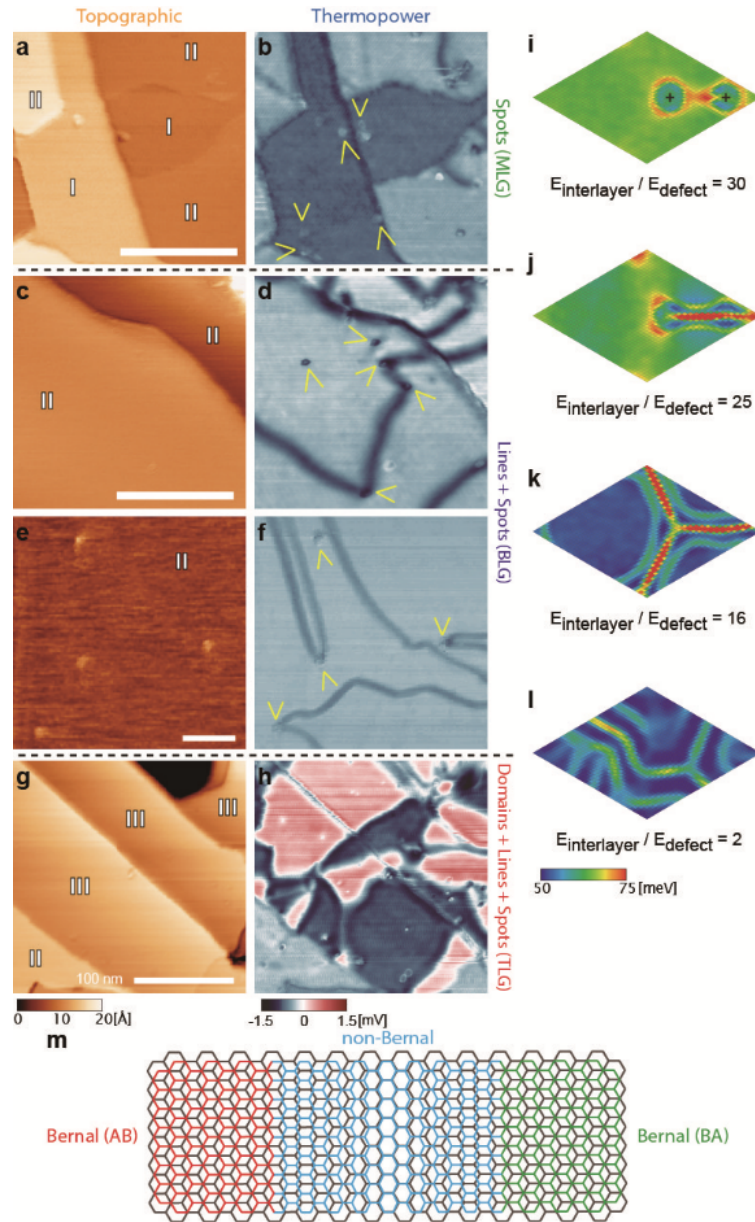


Figure 36. Evolution of strain-response patterns in epitaxial graphene. The columns a,c,e,g and b,d,f,h are topographic and corresponding thermopower images, respectively. a,b are from MLG; c,f are from BLG; g,h are from TLG. In a flat region of BLG (e-f), the dark spots in f (yellow arrows) correspond to the buckled spots in the

topographic image, e. (i)-(l) Simulated strain energy maps showing how graphene sheets with (40×40) unit cells accommodate a given compressive strain.

It is known that materials synthesis involves a variety of processes that generate stress in the solid. Materials respond to stress in different ways, creating a diversity of structural imperfections and strain in the lattice, which have their origins at the atomic level. Detecting these subtle features with high sensitivity and resolution, and their influence on electronic, thermal, and mechanical properties, remains challenging. Scanning probe methods, particularly tunnelling microscopy, have been useful to measure such properties locally. However, standard measurements are not well suited to finding the small changes in lattice parameters that accompany strain and disorder, and large-scale imaging of the associated electronic states is prohibitive. Disorder and strain can have large and spatially localized electronic signatures, even for subtle changes in atomic positions.

As preliminary tested in Figure 8, thermoelectric scanning measurement was exploited and proved capable of detecting these signatures with an enhanced sensitivity even down to an atomic-scale. Based on the success of thermoelectric imaging, more detailed analysis has been given in order to image structural disorder of the epitaxial graphene. Figure 36(b), (d), and (f) show close-up scans of the complex features in the thermopower images, where the patterns evolve from spots in MLG into line patterns in BLG. Despite their strikingly explicit contrast in the thermopower images, these patterns are either subtle or unobservable in the topographic images [Figure 36 (a), (c), (e), and (g)]. The variation of the patterns, found to be dependent on the number of graphene layers, is reminiscent of the stress relaxation patterns observed in metal epitaxy studies. The evolution of the surface structure indicates that the phenomenon is driven by the free energy of the system, mainly the strain energy and the inter-layer cohesive energy.

We reproduced the tendency in pattern evolution by simulating the response patterns of graphene under compressive strain as a function of the interlayer cohesive energy with the Metropolis Monte Carlo algorithm. Figure 36(i)-(l) illustrates how a (40×40) unit cell graphene system containing two defect sites, which have weaker interlayer cohesive energy than other sites, accommodates a given uniform compressive strain into a non-uniform distribution. Generally, the observed response will be strain patterns following the overall trends in Figure 36(i)-(l). However, we postulate that the line patterns in BLG may represent strained boundary walls between different AB (Bernal) stacking domains [Figure 36(m)]. The resulting wall will be a compressively strained strip accommodating the different Bernal stacking sequences, namely AB and BA, in each neighbouring domain, and thus will contain transitional stacking sequences. This structure is a soliton domain wall. Recently, a Cornell group reported similar patterns from TEM study. The thermopower is negatively enhanced by more than a factor of two in the line patterns in BLG [Figures 8(c) and 36(d) and (f)], which we attribute to the additional local DOS above E_F due to the quantum confinement in the wall of width L , i.e. a quantization of the wave number k as $kL=n\pi$.

The potential of thermopower imaging persists at the atomic scale. Shown in Fig. 37 is an atomically-resolved image of BLG obtained near room temperature from both topographic [Figure 37(a)] and thermopower [Figure 37(b)] measurements. The AFM image [Figure 37(a)] shows atomic corrugation predominantly in one direction, with smaller amplitude along the corrugated rows, while the thermopower image in Figure 38(b) displays atomically resolved carbon hexagons in addition to the contrast related to the $6\sqrt{3} \times 6\sqrt{3} R30^\circ$ reconstruction of the underlying SiC lattice, reminiscent of STM images of this surface. These atomic variations were observable only when there was a finite temperature difference between the probe and the sample. This extremely localized probing is dependent on a sharp probe contact and the coherence in thermoelectric transport. We note that, the atomic resolution imaging by STM also relies on the local DOS, but with a different manner of dependency.

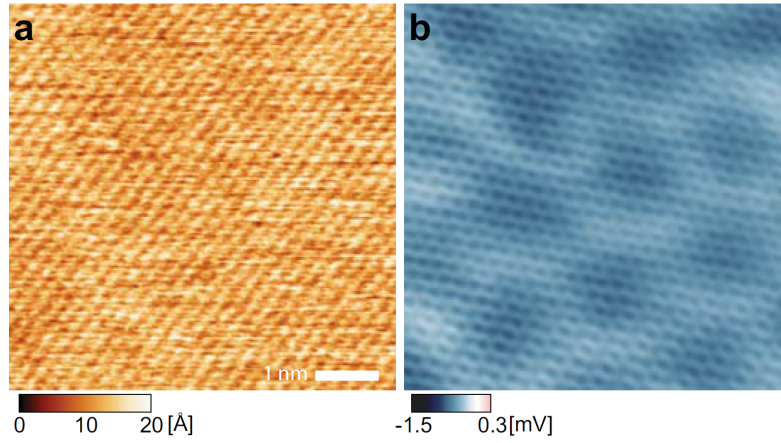


Figure 37. Thermoelectric imaging at the atomic scale. Atomically-resolved image of BLG obtained near room temperature from both (a) topographic and (b) thermopower measurements.

The atomic-scale imaging allows us to investigate and identify the structural disorder leading to the line patterns discovered by large-scale thermopower imaging. This procedure is demonstrated in Figure 38 where spots and line patterns are found at the nanoscale [Figure 38(a) and (b)] and a local defect is found in the close-up image at the joint intersecting line patterns [Figures 38(c) and 38(d)]. The AFM image [Figure 38(c)] shows that the number of (zigzag) atomic rows changes across the defect, which indicates the presence of a heptagon-pentagon pair, *i.e.* a dislocation core. This identification of a naturally existing dislocation core supports the suggested model of a soliton domain wall described in Figure 36(m). The simultaneously obtained thermopower image [Figure 38(d)] displays a complex interference pattern originating from electron scattering. The Fourier transform of this scattering image [inset of Figure 38(d)] suggests intervalley scattering of the electrons with a wave vector approximately equal to the Fermi wave vector. This electronic signature once again indicates that thermopower imaging reflects information of the local DOS.

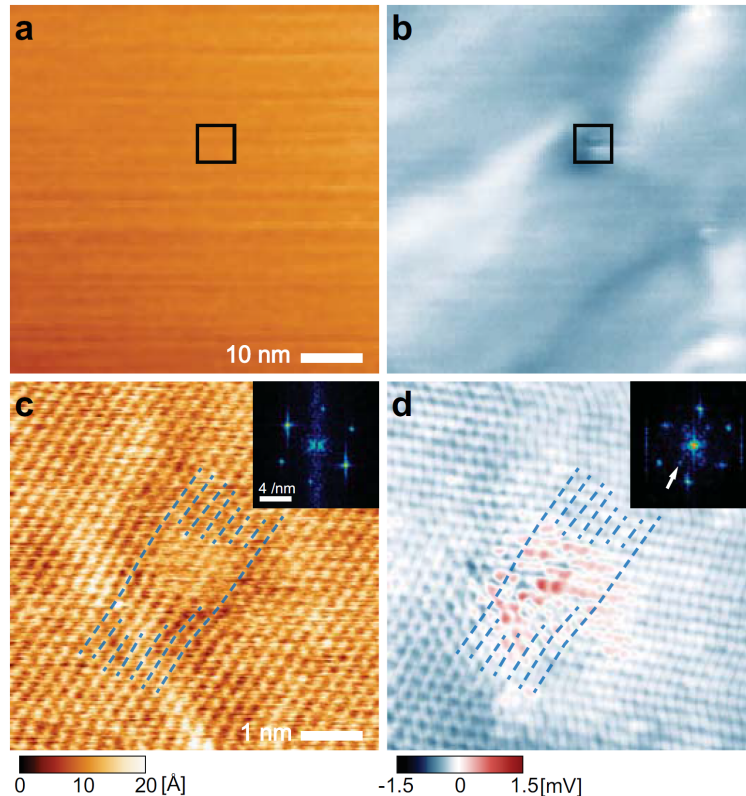


Figure 38. Local defect investigation by the thermoelectric imaging. (a) and (b) Spots and line patterns found at the nanoscale. (c) and (d) Close-up images at the joint intersecting line patterns.

The striking sensitivity and contrast of the strain related patterns in epitaxial graphene demonstrates the nature of thermopower measurements that amplify the variations in local DOS as if a physically-operated differential filter for the electronic states near E_F . Combined with the high throughput of our method, at the speed of conventional AFM, we can readily detect strain, defect variations within a material, and quantify their areal density. For instance, Figure 8(c) yields a defect site density on the order of 10^{10} cm^{-2} , a property challenging to determine with conventional methods.

Many future opportunities are opened with local measurements of thermopower. By controlling the Fermi-level of the sample through gating, measurements would be able to reveal information from a larger range of the energy bands. Furthermore, the Fermi-energy-sensitive nature enabled by a small temperature difference may be exploited in other spectroscopic measurements aimed to investigate the electronic structure, inspiring future novel measurement schemes.

In summary, the AOARD-KRF ‘thermal management’ project has led to several developments and breakthroughs driven by collaborative efforts between the Korean groups (Seoul National University and KRISS) and Brown University. Improved thermoelectric efficiency was achieved in several new material systems and by methods of nano-patterning and atomic-layer engineering. A novel “thermal diode” concept was implemented in and validated by experiments. A bio-inspired self-regulating cooling mechanism was developed and demonstrated in composite structure capable of synthetic sweating. An ultrathin ($\sim 40\text{nm}$) film that is infrared (heat) reflecting, light-transmitting ($>90\%$), highly conductive ($\sim 1000 \text{ S/cm}$) and also EMI-shielding ($>20\text{dB}$) was another example outcome of the exploration of an atomic-layer engineering approach developed in this project. One breakthrough – thermal-voltage imaging with unprecedented atomic resolution that exceeds classical limits is particularly noteworthy. It will likely extend its impact beyond thermal management into basic sciences for years to come.

These successes, however still preliminary, highlight the benefits and potential of the collaboration between Korean and USA research groups that were enabled by AOARD and KRF, and open doors to further advances in thermal management.

References

1. Ming Hu, Sergei Shenogin, Pawel Koblinski, and Nachiket Raravikar, “Air flow through carbon nanotube arrays”, *Appl. Phys. Lett.*, 91, 131905 (2007).
2. K. Kordás, G. Tóth, P. Moilanen, M. Kumpumäki, J. Vähäkangas, A. Uusimäki, R. Vajtai, and P. M. Ajayan, “Chip cooling with integrated carbon nanotube microfin architectures”, *Appl. Phys. Lett.*, 90, 123105 (2007).
3. T. H. Benzinger, “On physical heat regulation and the sense of temperature in man”, *Proc. Natl. Acad. Sci.*, 45, 645 (1959).
4. K Tauer, D Gau, S Schulze, A Volkel, and R Dimova, “Thermal property changes of poly(N-isopropylacrylamide) microgel particles and block copolymers”, *Colloid Polym. Sci.*, 287, 299 (2009).
5. Hyo-Sung Lee, Byung-Sung Kim, Hyun-Mi Kim, Jung-Sub Wi, Sung-Wook Nam, Kyung-Bae Jin, Yoshihiro Arai, and Ki-Bum Kim, “Electron beam projection nanopatterning using crystal lattice images obtained from high resolution transmission electron microscopy”, *Adv. Mater.*, 19, 4189 (2007).
6. Hyun-Mi Kim, Min Hyun Lee, Hyo-Sung Lee, Jung-Sub Wi, Kipil Lim, and Ki-Bum

- Kim, "Method of improving the quality of nanopatterning in atomic image projection electron-beam lithography", *J. Vac. Sci. Technol. B*, 27, 2553 (2009).
7. D. Roukevitch, T. Bigioni, M. Moskovits, and J. M. Xu, "Electrochemical fabrication of CdS nano-wire arrays in porous anodic aluminum oxide templates", *J. Phys. Chem.*, 100, 14037 (1996).
8. J. Li, C. Papadopoulos, M. Moskovits, and J. M. Xu, "Highly-ordered carbon nanotube arrays for electronics applications", *Appl. Phys. Lett.*, 75, 367 (1999).
9. J. Li, C. Papadopoulos, and J. M. Xu, "Y-junction carbon nanotubes and controlled growth", *Nature* 402, 253 (1999).
10. C. Papadopoulos, A. Rakitin, J. Li, A. S. Vedenev, and J. M. Xu, "Electronic transport in Y-junction carbon nanotubes", *Phys. Rev. Lett.*, 85, 3476 (2000).
11. S. K. Panda, D. Han, H. Yoo, H. Shin, H. Park, and J. Xu, "Synthesis of step-shaped bismuth nanowires - An approach towards the fabrication of self-homojunction", *Electrochem. Solid-State Lett.*, 14, E21 (2011).
12. D.-J. Lee, S.-S. Yim, K.-S. Kim, S.-H. Kim, and K.-B. Kim, "Formation of Ru nanotubes by atomic layer deposition onto an anodized aluminum oxide template", *Electrochem. Solid-State Lett.*, 11, K61 (2008).
13. S.-H. Park, S. Kim, D.-J. Lee, S. Yun, Z. G. Khim, and K.-B. Kim, "Selective wet-chemical etching of the barrier layer during formation of porous anodic aluminum oxide template", *J. Electrochem. Soc.*, 156, K181 (2009).
14. D.-J. Lee, H.-M. Kim, J.-Y. Kwon, H. Choi, S.-H. Kim, and K.-B. Kim, "Structural and electrical properties of atomic layer deposited Al-doped ZnO films", *Adv. Funct. Mater.*, 21, 448 (2011).
15. D.-J. Lee, J.-Y. Kwon, S.-H. Kim, H.-M. Kim, and K.-B. Kim, "Effect of Al distribution on carrier generation of atomic layer deposited Al-doped ZnO films", *J. Electrochem. Soc.*, 158, D277 (2011).
16. Do-Joong Lee, Ki-Ju Kim, Soo-Hyun Kim, Jang-Yeon Kwon, Jimmy Xu, and Ki-Bum Kim, "Atomic layer deposition of Ti-doped ZnO films with enhanced electron mobility", *J. Mater. Chem. C* (in press).
17. Jackson He, "Datacenter Power Management: Power Consumption Trend" <http://communities.intel.com/community/datastack/blog/2008/02/20/datacenter-power-management-power-consumption-trend>, February 20 (2008).
18. Seungwoo Jung, Ki-Bum Kim, Gustavo Fernandes, Jin Ho Kim, Fazal Wahab and Jimmy Xu, "Enhanced thermoelectric power in nanopatterned carbon nanotube film", *Nanotechnology*, 23, 135704 (2012).
19. A. Boltasseva and H. A. Atwater, "Low-Loss Plasmonic Metamaterials", *Science*, 331, 290 (2011).
20. M. A. Noginov, Lei Gu, J. Livenere, G. Zhu, A. K. Pradhan, R. Mundle, M. Bahoura, Yu. A. Barnakov, and V. A. Podolskiy, "Transparent conductive oxides: Plasmonic materials for telecom wavelengths", *Appl. Phys. Lett.*, 99, 021101 (2011).
21. G. V. Naik, J. Liu, A. V. Kildishev, V. M. Shalaev, and A. Boltasseva, "Demonstration of Al:ZnO as a plasmonic component for near-infrared metamaterials", *Proc. Natl. Acad. Sci.*, 109, 8834 (2012).
22. G. E. Fernandes, D.-J. Lee, J. H. Kim, K.-B. Kim, and J. Xu, "Infrared and microwave shielding of transparent Al-doped ZnO superlattice grown via atomic layer deposition", *J. Mater. Sci.*, 48, 2536 (2013).
23. A. Rotzetter, C. Schumacher, S. Bubenhofer, R. Grass, L. Gerber, M. Zeltner, and W. Start, "Thermoresponsive polymer induced sweating surfaces as an efficient way to passively cool buildings," *Adv. Mater.*, 24, 5352 (2012).

List of Publications and Significant Collaborations that resulted from your AOARD supported project

a) papers published in peer-reviewed journals

1. Seungwoo Jung, Ki-Bum Kim, Gustavo Fernandes, Jin Ho Kim, Fazal Wahab, and Jimmy Xu, "Enhanced thermoelectric power in nanopatterned carbon nanotube film", *Nanotechnology*, 23, 135704 (2012).
2. Gustavo E. Fernandes, Do-Joong Lee, Jin Ho Kim, Ki-Bum Kim, and Jimmy Xu, "Infrared and microwave shielding of transparent Al-doped ZnO superlattice grown via atomic layer deposition", *J. Mater. Sci.*, 48, 2536 (2013).
3. Chih-Hsun Hsu and Jimmy Xu, "Diamond Nanowire – a challenge from the extremes", *Nanoscale*, 4, 5293 (2012).
4. Gustavo E. Fernandes, Jin Ho Kim, and Jimmy Xu, "Thermoelectric response of carbon nanotube films to Au-nanoparticle incorporation", *Mater. Res. Bull.*, on-line published (2013).
5. Do-Joong Lee, Ki-Ju Kim, Soo-Hyun Kim, Jang-Yeon Kwon, Jimmy Xu, and Ki-Bum Kim, "Atomic layer deposition of Ti-doped ZnO films with enhanced electron mobility", accepted to *J. Mater. Chem. C* (2013).
6. G.E. Fernandes, J-H Kim, A. Sood, and J.M. Xu, "Giant temperature coefficient of resistance in carbon nanotube / phase-change polymer nanocomposites", *Adv. Func. Mater.*, on-line published (2013).
7. S. D. Kang, S. C. Lim, E.-S. Lee, Y. W. Cho, Y.-H. Kim, H.-K. Lyee, and Y. H. Lee, "Interfacial thermal conductance observed to be higher in semiconducting than metallic carbon nanotubes", *ACS Nano*, 6, 3853 (2012).
8. S. Cho, S. D. Kang, W. Kim, E.-S. Lee, S.-J. Woo, K.-J. Kong, I. Kim, H.-D. Kim, T. Zhang, J. A. Strosio, Y.-H. Kim, and H.-K. Lyee, "Thermoelectric imaging of structural disorder in epitaxial graphene", arXiv:1305.2845, *Nature Materials*, accepted (2013).

b) papers published in peer-reviewed conference proceedings

1. Gustavo Fernandes, Do-Joong Lee, Jin Ho Kim, Seungwoo Jung, Gi-Yong Jung, Fazal Wahab, Youngok Park, Ki-Bum Kim, and Jimmy Xu, "Nano-heterogeneous structuring effects on thermal power factor and thermal conductivity", *Materials Challenges in Alternative and Renewable Energy II*, Ceramic Transactions vol. 239, pp. 225-233, Wiley (2013).

d) conference presentations

1. Seungwoo Jung, Gustavo Fernandes, Jin Ho Kim, Ki-Bum Kim, and Jimmy Xu, "Enhanced Thermopower in CNT Film with Nanopatterning", 2011 MRS Fall meeting, November 2012.
2. Seungwoo Jung, G. Fernandes, Jin Ho Kim, Ki-Bum Kim, and Jimmy Xu, "Enhanced thermoelectric power in CNT film with nanopatterning", IEEE NMDC 2011, October 2011.
3. Do-Joong Lee, G. Fernandes, Jin Ho Kim, Ki-Bum Kim, A. Larocque, and Jimmy Xu, "AZO - An infrared-reflecting, EMI-shielding, highly-conductive, transparent compound

semiconductor”, WOCS-DICE-EXMATEC 2012, May 2012 (invited presentation).

4. Do-Joong Lee, Jang-Yeon Kwon, Soo-Hyun Kim, Ki-Ju Kim, Jimmy Xu, and Ki-Bum Kim, “ALD of transition metal doped ZnO Films for transparent electrode”, 12th International Conference on Atomic Layer Deposition (ALD 2012), June 2012.

5. Gi-Yong Chung, Stephen Dongmin Kang, Do-Joong Lee, Ho-Ki Lyeo, Jimmy Xu, and Ki-Bum Kim, “Electrical and thermal transport properties of atomic layer deposited Al-doped ZnO films”, 12th International Conference on Atomic Layer Deposition (ALD 2012), June 2012.

6. Do-Joong Lee, Jang-Yeon Kwon, Soo-Hyun Kim, Hyun-Mi Kim, Gustavo E. Fernandes, Jin Ho Kim, Jimmy Xu, and Ki-Bum Kim, “Layer-by-layer doped ZnO films grown by atomic layer deposition”, 2012 Materials Research Society (MRS) fall meeting, November 2012.

7. M.Y. Kang, M.H. Lee, H.-M. Kim, G. Fernandes, J. Xu, and K.-B. Kim, “Rectifying Optical Antenna Array-sensing and Light Energy Harvesting”, 25th International Microprocesses and Nanotechnology Conference (MNC), November 2012.

8. Jimmy Xu, (Plenary Speech) “Plasmonic Oxides – good transparent electrodes, great meta-optics, and extraordinary heat-conductor too?” Intl Conf on Electronic Materials and Nanotechnology for Green Environment, JeJu, Korea, September 16-19, 2012

e) manuscripts submitted but not yet published

1. Aaron Larocque, Jin Ho Kim, and Jimmy Xu, “Thermal rectification in phase change materials with temperature dependent thermal conductivity”, Applied Thermal Engineering, in submission

2. Aaron Larocque, Jin Ho Kim, Gustavo Fernandes, and Jimmy Xu, “Self-regulated cooling via synthetic sweating nanocomposites”, Advanced Materials, in submission

g) patents filed

1. Aaron Larocque, Jin Ho Kim, and Jimmy Xu. “Method and apparatus for cooling a thermal source” 61/68, 338, filed August 1, 2012.